



# **ICQNM 2019**

The Thirteenth International Conference on Quantum, Nano/Bio, and Micro  
Technologies

ISBN: 978-1-61208-749-8

October 27 - 31, 2019

Nice, France

## **ICQNM 2019 Editors**

Giovanna Calò, Polytechnic of Bari, Italy  
Gaetano Bellanca, University of Ferrara, Italy

# ICQNM 2019

## Forward

The Thirteenth International Conference on Quantum, Nano/Bio, and Micro Technologies (ICQNM 2019), held between October 27, 2019 and October 31, 2019 in Nice, France, continued a series of events started in 2015 and covering research in the field of software system integration.

Quantum technologies and nano technologies have a great potential to transform communications telecommunications infrastructure and communication protocols, and computers and networking devices. Nanotechnologies and micro-technologies already made their mark on smart materials, nano-medicine, nano-devices, molecular manufacturing, biotechnology, metrology, airspace.

The advancements in material science and computer science have allowed the building, launching and deploying of space exploration systems that continually do more and more as they become smaller and lighter. As an example, carbon nano-tubes have been created that are 250 times stronger than steel, 10 times lighter, and transparent. Similar advances are occurring in glass, plastics and concrete. Spacecraft are being launched, with hulls that are composed of carbon fibers, a light weight high strength material.

Swarms is another concept of nano-robotics; swarms act in unison like bees. They theoretically will act as a flexible cloth like material, as strong as diamond. Interplanetary exploration can be foreseen as being carried on by nano-robots as well.

Electronic devices, medicine, environment, metrology, aerospace programs, clothes and materials, telecommunications, cryptography, semiconductors, manufacturing, and other domains are impacted by the progress on the areas mentioned above. Particularly, micro imaging, nano-medicine: (drug delivery; nano-particles i.e. viruses; proteins.), bio-nanostructures: (nano-tubes, nano-particles), microsystems, micro fluidics: (including nano-fluidics, modeling; fabrication and application), micro instrumentation / implantable microdevices (miniaturized bio-electronic systems etc.) and micro sensors benefits from the progress on quantum, nano and micro technologies.

We take here the opportunity to warmly thank all the members of the ICQNM 2019 technical program committee, as well as all the reviewers. The creation of such a high quality conference program would not have been possible without their involvement. We also kindly thank all the authors who dedicated much of their time and effort to contribute to ICQNM 2019. We truly believe that, thanks to all these efforts, the final conference program consisted of top quality contributions.

We also thank the members of the ICQNM 2019 organizing committee for their help in handling the logistics and for their work that made this professional meeting a success.

We hope that ICQNM 2019 was a successful international forum for the exchange of ideas and results between academia and industry and to promote further progress in the area of quantum, nano/bio, and micro technologies. We also hope that Nice, France provided a pleasant environment during the conference and everyone saved some time to enjoy the charm of the city.

### ICQNM 2019 Chairs

#### ICQNM Steering Committee

Sergey Yurish, IFSA, Spain

Shaya Fainman, University of California, San Diego, USA

Stefano Mancini, University of Camerino, Italy

Ashok Srivastava, Louisiana State University, Baton Rouge, USA  
Xin-Wei Yao, Zhejiang University of Technology, China  
Masahito Hayashi, Nagoya University, Japan

**ICQNM Research/Industry Committee**

Thierry Ferrus, Hitachi Cambridge Laboratory, UK  
Travis S. Humble, Oak Ridge National Laboratory, USA  
Christian Kollmitzer, AIT Austrian Institute of Technology GmbH, Austria  
Marco Genovese, Italian Metrological Institute (INRIM) -Torino, Italy  
Keiji Matsumoto, National Institute of Informatics, Japan

## **ICQNM 2019 Committee**

### **ICQNM Steering Committee**

Sergey Yurish, IFSA, Spain  
Shaya Fainman, University of California, San Diego, USA  
Stefano Mancini, University of Camerino, Italy  
Ashok Srivastava, Louisiana State University, Baton Rouge, USA  
Xin-Wei Yao, Zhejiang University of Technology, China  
Masahito Hayashi, Nagoya University, Japan

### **ICQNM Research/Industry Committee**

Thierry Ferrus, Hitachi Cambridge Laboratory, UK  
Travis S. Humble, Oak Ridge National Laboratory, USA  
Christian Kollmitzer, AIT Austrian Institute of Technology GmbH, Austria  
Marco Genovese, Italian Metrological Institute (INRIM) -Torino, Italy  
Keiji Matsumoto, National Institute of Informatics, Japan

### **ICQNM 2019 Technical Program Committee**

Qammer H. Abbasi, Texas A&M University at Qatar, Qatar  
Hossein Aghababa, University of Tehran, Iran  
Mohamed Atef, Assiut University, Egypt  
Nihar Athreyas, Spero Devices, Inc., USA  
Michael Taynnan Barros, IRC Government of Ireland | Telecommunications Software and Systems Group (TSSG) | Waterford Institute of Technology (WIT), Ireland  
Gaetano Bellanca, University of Ferrara, Italy  
V́ctor M. Castaño, Universidad Nacional Aut3noma de M3xico, Mexico  
Sang H. Choi, NASA Langley Research Center, USA  
Eugen Dedu, Univ. Bourgogne Franche-Comt3 / FEMTO-ST Institute / CNRS Montb3liard, France  
Shaya Fainman, University of California, San Diego, USA  
Thierry Ferrus, Hitachi Cambridge Laboratory, UK  
Marco Genovese, Italian Metrological Institute (INRIM) -Torino, Italy  
Olga Glukhova, Saratov State University, Russia  
Young-Geun Han, Hanyang University, Korea  
Masahito Hayashi, Nagoya University, Japan  
Liangxing Hu, Nanyang Technological University, Singapore  
Travis S. Humble, Oak Ridge National Laboratory, USA  
Kourosh Kalantar-Zadeh, Centre for Advanced Electronics and Sensors (CADES) | RMIT University, Melbourne, Australia  
Paul Kiekens, Ghent University, Belgium  
Christian Kollmitzer, AIT Austrian Institute of Technology GmbH, Austria  
Jun Li, Kansas State University, USA  
Jianlin Liu, University of California, Riverside, USA  
Jianjun Ma, Brown University, USA

Jorge Maestre Vidal, Complutense University of Madrid (UCM), Spain  
Stefano Mancini, University of Camerino, Italy  
Keiji Matsumoto, National Institute of Informatics, Japan  
Jose Manuel Molina Lopez, Universidad Carlos III de Madrid, Spain  
Mevludin Memedi, Örebro University, Sweden  
Drouiche Nadjib, Centre de Recherche en Technologie des Semi-conducteurs pour l'Energétique (CRTSE), Algeria  
Masaki Nakanishi, Yamagata University, Japan  
Ki-Hwan Nam, Korea Basic Science Institute (KBSI), Korea  
Hock Chun Ong, Chinese University of Hong Kong, Hong Kong  
Nadras Othman, Universiti Sains Malaysia, Malaysia  
Victor Ovchinnikov, Aalto University, Finland  
Telhat Ozdogan, Amasya University, Turkey  
Kwangjin Park, Wonkwang University, South Korea  
Salvatore Petralia, ADG Central R&D | STMicroelectronics, Italy  
Peter Schartner, University of Klagenfurt, Austria  
Stefan Schauer, AIT Austrian Institute of Technology GmbH - Vienna, Austria  
O.L. Shanmugasundaram, K.S.Rangasamy College of Technology, India  
Parvinder Singh, Deenbandhu Chhotu Ram University of Science and Technology, Murthal, India  
Maciej Sitarz , AGH University of Science and Technology, Poland  
Marco Antonio Sotelo Monge, Universidad Complutense de Madrid, Spain  
Sandro Sozzo, University of Leicester, UK  
Ashok Srivastava, Louisiana State University, Baton Rouge, USA  
Ivo Stachiv, Harbin Institute of Technology, Shenzhen China & Institute of Physics - Czech Academy of Sciences, Prague, Czech Republic  
Eric Suraud, Université Paul Sabatier, France  
Michael Taynnan Barros, IRC Government of Ireland | Telecommunications Software and Systems Group (TSSG) | Waterford Institute of Technology (WIT), Ireland  
Pramod K. Tiwari, Indian Institute of Technology (IIT) Patna, India  
Salvador Elias Venegas-Andraca, Tecnológico de Monterrey, Mexico  
Robert Wille, Institute for Integrated Circuits | Johannes Kepler University, Linz, Austria  
Xin-Wei Yao, Zhejiang University of Technology, China  
Sergey Yurish, IFSA, Spain  
Katerina Zaharieva, Institute of Catalysis | Bulgarian Academy of Sciences, Bulgaria  
Alexander Zhanov, Gwangju Institute of Science and Technology (GIST), Republic of Korea

## Copyright Information

For your reference, this is the text governing the copyright release for material published by IARIA.

The copyright release is a transfer of publication rights, which allows IARIA and its partners to drive the dissemination of the published material. This allows IARIA to give articles increased visibility via distribution, inclusion in libraries, and arrangements for submission to indexes.

I, the undersigned, declare that the article is original, and that I represent the authors of this article in the copyright release matters. If this work has been done as work-for-hire, I have obtained all necessary clearances to execute a copyright release. I hereby irrevocably transfer exclusive copyright for this material to IARIA. I give IARIA permission to reproduce the work in any media format such as, but not limited to, print, digital, or electronic. I give IARIA permission to distribute the materials without restriction to any institutions or individuals. I give IARIA permission to submit the work for inclusion in article repositories as IARIA sees fit.

I, the undersigned, declare that to the best of my knowledge, the article does not contain libelous or otherwise unlawful contents or invading the right of privacy or infringing on a proprietary right.

Following the copyright release, any circulated version of the article must bear the copyright notice and any header and footer information that IARIA applies to the published article.

IARIA grants royalty-free permission to the authors to disseminate the work, under the above provisions, for any academic, commercial, or industrial use. IARIA grants royalty-free permission to any individuals or institutions to make the article available electronically, online, or in print.

IARIA acknowledges that rights to any algorithm, process, procedure, apparatus, or articles of manufacture remain with the authors and their employers.

I, the undersigned, understand that IARIA will not be liable, in contract, tort (including, without limitation, negligence), pre-contract or other representations (other than fraudulent misrepresentations) or otherwise in connection with the publication of my work.

Exception to the above is made for work-for-hire performed while employed by the government. In that case, copyright to the material remains with the said government. The rightful owners (authors and government entity) grant unlimited and unrestricted permission to IARIA, IARIA's contractors, and IARIA's partners to further distribute the work.

## Table of Contents

Cavity Resonator Integrated Grating Filters: Recent Advances for Laser Wavelength Stabilization and Enhanced Second Harmonic Generation <i>Antoine Monmayrant, Olivier Gauthier-Lafaye, Stephane Calvez, Francois Renaud, Anne-Laure Fehrembach, and Evgueni Popov</i>	1
Plasmonic Nano-tweezers for Dielectric or Metallic Nano-objects Trapping <i>Djeber Guendouz, Pierrick Lample, Giovanni Magno, Beatrice Dagens, Vy Yam, and Giovanna Calo</i>	5
Differential Optical Sensing through Coupled Micro Ring Resonators <i>Ali Emre Kaplan, Gaetano Bellanca, and Paolo Bassi</i>	7
True Random Number Generation with Beam Splitters under Combined Input Scenarios using Defined Quantum States to Increase the Security of Cryptographic Devices <i>Martin Suda, Gerald Dissauer, and Florian Prawits</i>	11
Analysis, Design and Performance Evaluation of On-Chip Optical Wireless Links <i>Jinous Shafiei Dehkordi, Velio Tralli, Marina Barbiroli, Jacopo Nanni, Franco Fuschini, and Vincenzo Petruzzelli</i>	17
High Circular Dichroism Through Planar Plasmonic Metasurfaces and Enhancement through Surface Plasmon Resonances <i>Badrul Alam, Andrea Veroli, Vincenzo Petruzzelli, Luca Maiolo, Lorenzo Dominici, Francesco Todisco, Milena De Giorgi, Giorgio Pettinari, Annamaria Gerardino, and Alessio Benedetti</i>	23

# Cavity Resonator Integrated Grating Filters : Recent Advances for Laser Wavelength Stabilization and Enhanced Second Harmonic Generation

Antoine Monmayrant,  
Olivier Gauthier-Lafaye,  
Stéphane Calvez

LAAS-CNRS,  
Université de Toulouse, CNRS,  
F-31400 Toulouse, France  
email: antoine.monmayrant@laas.fr  
email: olivier.gauthier-lafaye@laas.fr  
email: stephane.calvez@laas.fr

François Renaud,  
Anne-Laure Fehrembach,  
Evgueni Popov

Aix Marseille Univ, CNRS  
Centrale Marseille, Institut Fresnel,  
F-13013 Marseille, France  
email: francois.renaud@fresnel.fr  
email: anne-laure.fehrembach@fresnel.fr  
email: e.popov@fresnel.fr

**Abstract**—Cavity Resonator Integrated Grating Filters (CRIGFs) are a peculiar mix between microcavities and Guided-Mode Resonant Filters (GMRFs). They rely on the coupling of free-space beams to guided and localized modes in a multilayer structure by subwavelength gratings. They provide spectrally selective reflection for tightly focussed beams, combining high Q-factors with high angular and positioning tolerances. Recently, their unusual properties have been harnessed to design and demonstrate compact and robust Extended Cavity Diode Lasers (ECDL) with single-mode and narrow-linewidth emission in the near infrared and Extended Cavity Quantum Cascade Lasers (ECQCL) with tunable emission in the mid-infrared. More recent works have taken advantage of new geometries on thermo-optic and non-linear material to demonstrate thermal tuning and second harmonic generation at telecom wavelengths. In this contribution, the principle and key features of CRIGFs will be presented together with the applications listed above.

**Keywords**—Bragg gratings; nanophotonics; optical filters.

## I. INTRODUCTION

Cavity Resonator Integrated Grating Filters (CRIGFs) have been introduced a few years ago as small aperture spectral filters [1]. Contrary to the Guided-Mode Resonant Filters (GMRFs) they are derived from, they exhibit large angular acceptance together with a filtered wavelength that does not depend on the conditions of incidence [2][3]. This opens the way to new geometries for extended cavities to stabilize the emitted wavelength of different kinds of lasers [4][5]. Here, we will report on recent advances on the CRIGF-based extended cavity diode laser and quantum cascade lasers.

The rest of the paper is structured as follows. Section II presents the main theoretical differences between CRIGFs and the more widespread GMRFs. Section III presents the use of CRIGFs for wavelength stabilization in extended cavities for both diode lasers (in the near infrared) and quantum cascade lasers (in the mid-infrared). Section IV details the recent approaches for wavelength tuning of CRIGFs, which are inherently fixed wavelength filters. We conclude our work in Section V.

## II. GMRFS AND CRIGFS THEORY

### A. GMRFs

GMRFs are based on the coupling of guided modes and propagating waves through Bragg gratings, usually called Grating Couplers (GCs). As described in Figure 1 (a), GMRFs are commonly based on a multistack layer that plays a double role around the wavelength of interest  $\lambda_0$  and the angle of incidence of interest  $\theta_0$ : (1) they act as an antireflection coating for incoming propagating waves; (2) they contain a single-mode planar waveguide (usually for TE guided-mode).

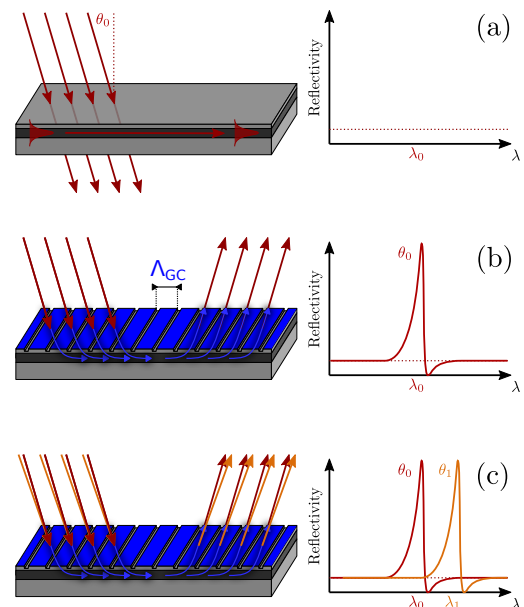


Figure 1. Principle of GMRFs: (a) base antireflection multistack layer; (b) grating coupler and Fano reflection spectrum; (c) angular tuning of the spectrum.

The GC is designed such that it couples the incoming propagating waves to the guided-mode at the wavelength of

interest  $\lambda_0$  (see Figure 1 (b)). Out of resonance (i.e., away from  $\lambda_0$ ), the reflectivity of the multistack is unaffected and stays low. At resonance, the incoming wave is simultaneously coupled into the waveguide and decoupled into the specular direction (see Figure 1 (b)). In the specular direction, this results in a Fano-shaped resonant spectrum that adds to the low reflectivity background. As the coupling condition of the incoming wave to the guided mode by the GC depends on the angle (Bragg condition), the spectral response can be tuned by changing the angle of incidence (see Figure 1 (c)), with a quasi-linear tuning for angles away from normal incidence (and quadratic tuning near normal incidence). The main design parameters of the GMRF (once the multistack and thus the waveguide are set) are the periodicity  $\Lambda_{GC}$  of the GC and its filling factor. The filling factor alters the width of the Fano resonance: the sharpest resonances are obtained for filling factors of 0.5 and the width of the resonance increases as we move away from 0.5. For a given angle of incidence and a given guided mode, the periodicity  $\Lambda_{GC}$  sets the wavelength of resonance  $\lambda_0$ . If we neglect the chromatic dispersion of the waveguide,  $\lambda_0$  scales linearly with the periodicity of the GC. One noticeable consequence of the angular tuning is the lack of angular tolerance of GMRFs with high-Q factors. For a high-Q factor GMRF, the spectral Fano peak is extremely narrow, and because of the linear angular tuning, this corresponds to a narrow angular tolerance. As a result, a high-Q GMRF results in a narrow spectral peak with high reflectivity only if (1) the incoming beam is large enough, with a flat phase-front (i.e., really close to an ideal plane wave); (2) the GMRF is large enough and perfectly uniform across its whole area. Any deviation from this ideal case results in reduced performance [6].

### B. CRIGFs

CRIGFs [1] are a variation around the concept of GMRFs. The base idea was to provide the same kind of spectral high-Q filter, but with a smaller footprint. The base geometry is depicted on Figure 2 (a).

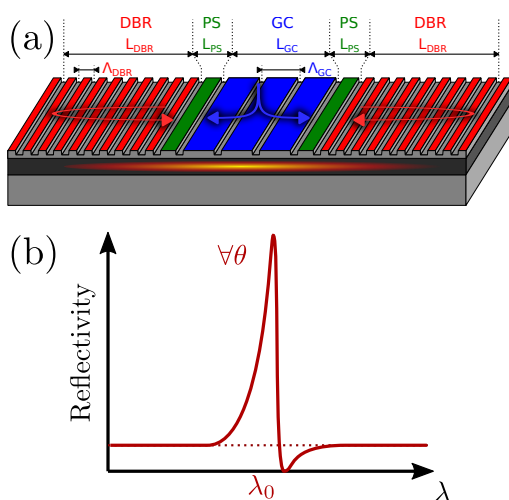


Figure 2. Principle of CRIGFs: (a) Schematic view of a CRIGF (b) Typical spectral reflectivity.

A small grating coupler (GC, in blue) of typically a few to a few tens of periods  $\Lambda_{GC}$  is sided by two unstructured Phase

Sections (PS, in green) and two Distributed Bragg Reflectors (DBR, in red). The pair of DBRs forms a planar Fabry-Pérot cavity that supports several modes, all localized under the GC. By adjusting the length  $L_{PS}$  of the phase section, one can ensure that one of these modes is spectrally overlapped with the Bragg resonance of the GC. When this is the case, a beam tightly focussed to the dimension  $L_{GC}$  of the GC, under normal incidence, can couple to this localized mode and re-emits along both the reflected and transmitted directions. As shown in Figure 2 (b), this coupling and re-emission results in one single Fano resonance at the wavelength of interest  $\lambda_0$ . Contrary to GMRFs, this spectrum is not tunable with the angle of incidence, the spectral reflectivity being set once and for all [7]. In particular, contrary to GMRFs where spectral and angular width are totally coupled, the CRIGF spectral width is decoupled from its angular acceptance. High-Q CRIGFs with large angular tolerances have been demonstrated [2]. Moreover, another distinction is that neither the spectral width, nor the spectral position of the resonance are affected by the conditions of incidence on the CRIGF [2][3]. The only parameter affected is the peak reflectivity that is maximized when the beam is spatially overlapped with the GC and when its size matches  $L_{GC}$ . One can thus tailor the size  $L_{GC}$  of the GC at the centre of the CRIGF to match that of the targeted focussed beam independently from the wavelength of interest and spectral width. One particular advantage of the CRIGF is its large tolerance [2] for both angular (several degrees) and positional (from few  $\mu\text{m}$  to few  $100\mu\text{m}$ ) degrees of freedom. One last property of the CRIGF that helps integrate several CRIGFs with different reflected wavelengths on a same substrate is that every critical dimension is directly proportional to the GC periodicity  $\Lambda_{GC}$ . Indeed, the DBR periodicity is  $\Lambda_{DBR} = 1/2\Lambda_{GC}$  and the optimal PS length was found to be  $L_{PS} = 1.125\Lambda_{GC}$  (see reference [2]). As the wavelength of interest  $\lambda_0$  is proportional to the GC periodicity  $\Lambda_{GC}$ , it is straightforward to design several CRIGFs at different wavelengths: one just needs to scale all the planar dimensions of the CRIGF (i.e.,  $\Lambda_{GC}$ ,  $\Lambda_{DBR}$ ,  $L_{PS}$ ) uniformly.

### III. CRIGFs FOR LASER WAVELENGTH STABILIZATION

#### A. Extended Cavity Diode Laser in the near infrared

One application of CRIGFs is the conception of minimalist Extended Cavity Diode Lasers (ECDLs), as reported in [4]. The goal of an ECDL is to enhance the spectral purity of a diode laser. The base principle of ECDL is two-fold: (1) the Fabry-Pérot cavity extends the laser beyond the length of the diode laser chip and thus decreases the spectral width of each Fabry-Pérot mode ; (2) a spectral filtering element introduced in the cavity further reduces the spectral width and selects one isolated mode. The ECDL is usually quite complex, tricky to align and not robust towards misalignment and vibrations, for two reasons. First, the ECDL contains many independent components (gain chip, several intracavity lenses, a spectral filter, an end reflector) that should all be carefully aligned. This makes the cavity more complex: more elements in the cavity means more elements to align and a reduction of the robustness of the cavity as each element is a possible point of failure. Second, most usual spectral filters with a high Q-factor (i.e., a low spectral width) only work efficiently on well collimated beams. The highly divergent output of the diode laser gain chip thus needs to be carefully collimated intracavity before

reaching the filtering element (as in the Littrow configuration, for example). This geometry is particularly sensitive to angular misalignment of the filter that hinders the optical feedback into the gain chip.

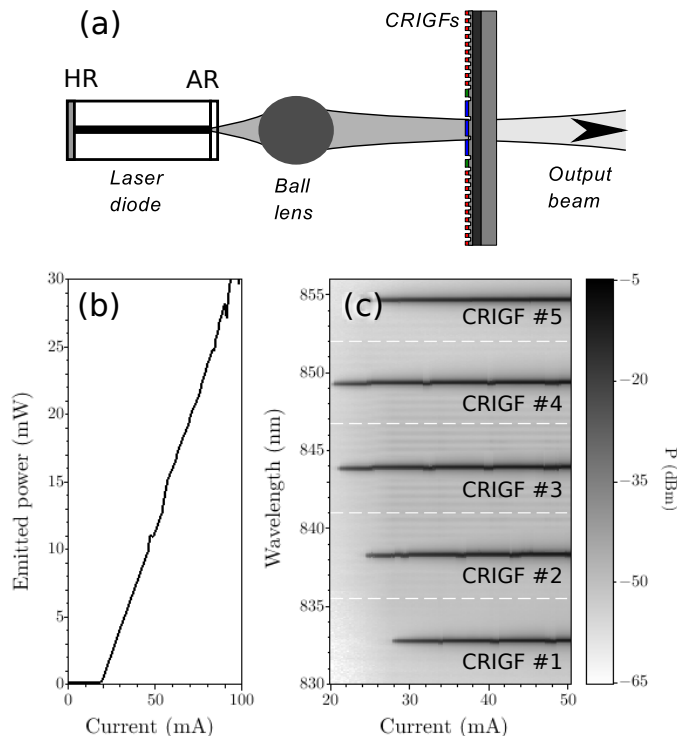


Figure 3. ECDL wavelength stabilization with CRIGFs: (a) schematic of the minimalist cavity; (b) Typical light curve; (c) Spectrum as a function of the injected current for 5 different CRIGFs.

As shown in Figure 3 (a), a CRIGF-based ECDL can be simpler than an usual ECDL. First, as the CRIGF acts simultaneously as the end reflector and the optical filter, the cavity only contains 3 elements: a gain chip, an imaging lens and the CRIGF. This reduces the number of elements in the ECDL and thus decreases the chances of failure. Second, as the CRIGF can work with tightly focused beams, the cavity has a so-called “cat’s-eye” geometry where the anti-reflection-coated facet of the gain chip (AR) is imaged onto the CRIGF that plays the role of a spectrally selective end reflector. This geometry is more robust towards angular displacement of the end reflector.

Figure 3 (b) shows a typical light curve (emitted power as a function of the injected current in the diode laser gain chip) for a CRIGF-based ECDL operating around 850 nm: thresholds around 20 mA and emitted power up to 30 mW are routinely achieved [4]. As can be seen in Figure 3 (c) that shows the emitted spectrum of the CRIGF-based ECDL as a function of the injected current for 5 different CRIGFs, depending on the spectral peak reflectivity of the CRIGF used, the emitted wavelength can be stabilized around any wavelength in the spectral gain of the diode laser. From Figure 3 (c), one can observe the detuning between the stabilization wavelength set by the CRIGF and the spectral gain of the diode laser: the higher the detuning, the higher the threshold. The smallest detuning is around 850 nm (the smallest threshold).

Current works in this field are focussing on miniaturization

of the cavity to fit all components in a butterfly package and on the achievement of low-linewidth emission [8] (few 100 kHz linewidth).

### B. Extended Cavity Quantum Cascade Laser in the mid-infrared

The stabilization of laser diodes described previously can be easily extended towards other wavelength ranges, like the mid-infrared. Indeed, there is nothing that is wavelength specific in the principle of CRIGFs. Provided that we find suitable materials (i.e., materials that we can process in a clean room and with appropriate refractive index and low absorption), we can design and fabricate CRIGFs in any wavelength ranges. In the mid-infrared, CRIGFs were demonstrated using GaAs/GaAlAs material system [5]. As presented in Figure 4, the geometry is exactly the same than in the near infrared. The only differences are due to the different wavelength range of operation: the gain chip is a quantum cascade gain chip, the optics are made of ZnSe and the CRIGF is GaAs/GaAlAs.

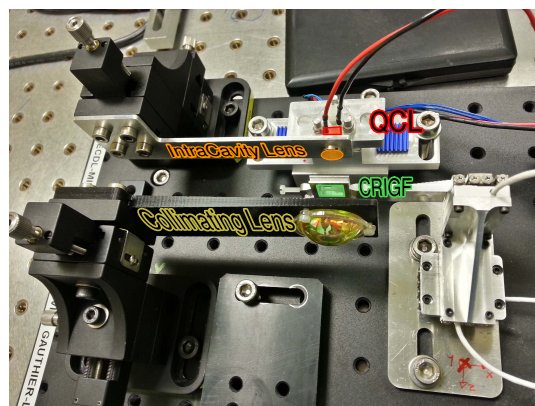


Figure 4. Extended cavity quantum cascade laser.

Figure 5 shows the spectrum emitted by the cavity as a function of the periodicity of the CRIGF used for stabilization. Each periodicity results in a particular wavelength reflected by the CRIGF. When the reflected wavelength is not too far detuned from the spectral gain of the quantum cascade gain chip (periodicity in the range [1460:1510] from red to light blue in Figure 5), the emission is stabilized to the reflected wavelength. When the detuning is too large (periodicity in the range [1520:1560] from blue to purple in Figure 5), the cavity emits around the maximum of the spectral gain and the emission is not stabilized.

### IV. TUNABLE CRIGFs: SPATIAL AND THERMAL TUNING

The main advantage of the CRIGFs (the reflected wavelength not depending on the conditions of incidence) is also a main disadvantage for some applications: the CRIGF is inherently non-tunable. Indeed, for both ECDL and ECQCL, in addition to wavelength stabilization, wavelength tuning would be beneficial. Two approaches have been followed. The first one takes advantage of the 2D nature of the CRIGF. As can be seen in Figure 2 (a), the CRIGF is invariant along the grooves of the GC and DBRs: along this dimension, the CRIGF can be arbitrarily long without noticeably changing the CRIGF properties. As the spectral reflectivity of the CRIGF is directly given by the planar dimensions ( $\Lambda_{GC}$ ,  $\Lambda_{DBR}$ ,  $L_{PS}$ ), one can

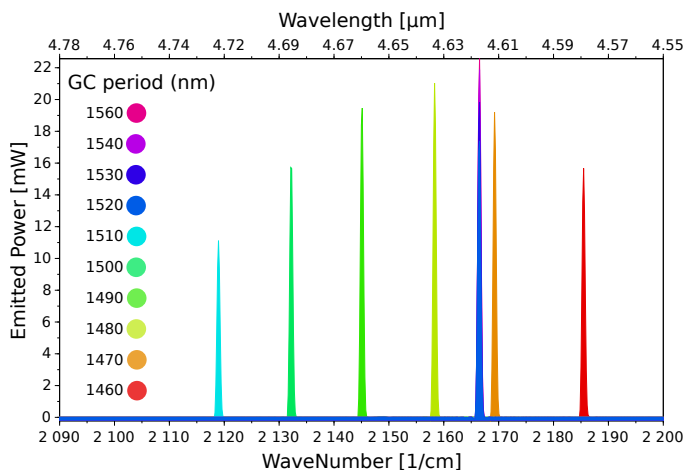


Figure 5. Wavelength stabilization of quantum cascade laser: emitted spectrum of the ECQCL as a function of the periodicity of the CRIGF used for stabilization.

introduce a gradient of these dimensions along the grooves of the GC [9].

Figure 6 (a) shows the image of a fabricate CRIGF with a gradient where the dimensions are scaled linearly along the  $y$ -dimension (along the groove direction). The wavelength of the spectral peak reflected by such a CRIGF (Figure 6 (b)) depends on the position along the  $y$ -direction. By spatially scanning the position along this direction, one can tune the reflected wavelength, the slope of the tuning depending on the strength of the gradient applied to the dimensions (from no gradient in red to strongest gradient in purple).

The second approach relies on thermo-optic materials. By using a thin film of  $\text{LiNbO}_3$  for the waveguide (that is a strongly non-linear, electro-optic and thermo-optic material), one can achieve tuning by altering the temperature of the substrate. Extremely recent results on thermally tuned CRIGFs working at telecom wavelengths [10][11] have demonstrated movement-free tuning over 2.4 nm for a temperature change of  $60^\circ$ . In addition, preliminary observation of second harmonic generation enhancement by CRIGF in such material has been reported[12].

## V. CONCLUSION

This contribution details the base principles of Guided Modes Resonant Filters (GMRFs) and Cavity Resonator Integrated Grating Filters (CRIGFs) and presents several applications of CRIGFs to laser wavelength stabilization. Recent results on CRIGF wavelength tuning using spatial gradients or thermally active materials are also discussed.

## ACKNOWLEDGMENT

F. Renaud acknowledges PhD grant from DGA/AID. Authors thankfully acknowledge the LAAS clean room team for technical support and technological expertise provided within the French RENATECH framework.

## REFERENCES

[1] K. Kintaka et al., "Cavity-resonator-integrated guided-mode resonance filter for aperture miniaturization," *Opt. Express*, vol. 20, no. 2, Jan. 2012, pp. 1444–1449.

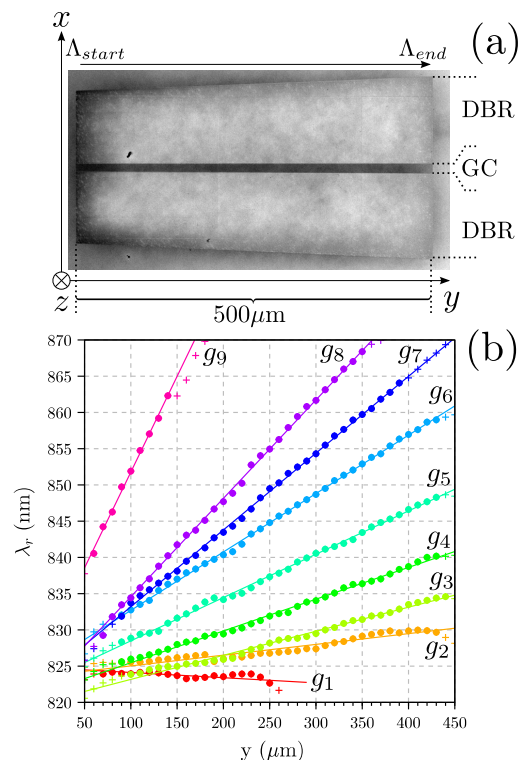


Figure 6. CRIGF with a spatial gradient: (a) top-view of a graded CRIGF; (b) Local spectral reflectivity as a function of the strength of the dimension gradient (from no gradient in red to strongest gradient in purple).

- [2] X. Buet et al., "High angular tolerance and reflectivity with narrow bandwidth cavity-resonator-integrated guided-mode resonance filter," *Opt. Express*, vol. 20, no. 8, Apr. 2012, pp. 9322–9327.
- [3] N. Rassem, A.-L. Fehrembach, and E. Popov, "Waveguide mode in the box with an extraordinary flat dispersion curve," *J. Opt. Soc. Am. A*, vol. 32, no. 3, Feb. 2015, pp. 420–430.
- [4] X. Buet et al., "Wavelength-stabilised external-cavity laser diode using cavity resonator integrated guided mode filter," *Electronics Letters*, vol. 48, no. 25, Dec. 2012, pp. 1619–1621.
- [5] S. Augé et al., "Mid-infrared cavity resonator integrated grating filters," *Optics Express*, vol. 26, no. 21, 2018, pp. 27 014–27 020.
- [6] A.-L. Fehrembach et al., "Measurement and modeling of 2d hexagonal resonant-grating filter performance," *J. Opt. Soc. Am. A*, vol. 27, no. 7, Jul. 2010, pp. 1535–1540.
- [7] R. Laberdesque et al., "High-order modes in cavity-resonator-integrated guided-mode resonance filters (crigfs)," *J. Opt. Soc. Am. A*, vol. 32, no. 11, Nov. 2015, pp. 1973–1981.
- [8] A. Monmayrant et al., "Cavity resonator integrated filter (CRIGF) based external cavity laser in a butterfly package," in 2019 21st International Conference on Transparent Optical Networks (ICTON). IEEE, Jul. 2019.
- [9] S. Augé, A. Monmayrant, S. Pelloquin, J. B. Doucet, and O. Gauthier-Lafaye, "Tunable graded cavity resonator integrated grating filters," *Optics Express*, vol. 25, no. 11, May 2017, pp. 12 415–12 420.
- [10] S. Calvez, A. Monmayrant, and O. Gauthier-Lafaye, "Lithium-niobate-based Cavity Resonator-Integrated Guided-mode Resonance Filters," Jun. 2019, poster.
- [11] S. Calvez, A. Monmayrant, and O. Gauthier-Lafaye, "Towards high-speed tuning Cavity Resonator-Integrated Guided-mode Resonance Filters," in EOS Topical meeting on Diffractive Optics 2019, Jena, Germany, Sep. 2019.
- [12] F. Renaud et al., "Second-harmonic-generation enhancement in cavity resonator integrated grating filters," *Opt. Lett.*, vol. 44, no. 21, Nov 2019, pp. 5198–5201.

## Plasmonic Nano-Tweezers for Dielectric or Metallic Nano-Objects Trapping

Djeber Guendouz, Pierrick Lample, Giovanni Magno,  
 Béatrice Dagens and Vy Yam  
 Center of Nanosciences and Nanotechnologies, CNRS,  
 University Paris-Sud  
 Palaiseau, France  
 e-mail: djeber.guendouz@u-psud.fr,  
 pierrick.lample@etudiant.univ-brest.fr, giovanni.magno@u-  
 psud.fr, beatrice.dagens@u-psud.fr, vy.yam@u-psud.fr

Giovanna Calò  
 Department of Electrical and Information Engineering,  
 Polytechnic of Bari  
 Bari, Italy  
 e-mail: giovanna.calo@poliba.it

**Abstract**— Optical tweezing is an emerging application of plasmonic nanostructures that aims at the exploitation of the enhanced light-matter interaction to trap nano-objects for sensing, biosensing, and spectroscopy purposes. In this contribution, we report the numerical analysis of efficient tweezing of subwavelength nanoparticles with radii smaller than 50 nm, in localized surface plasmon nanoantennas strongly coupled with Silicon on Insulator (SOI) waveguides. This integrated scheme ensures an intense excitation of the plasmonic resonators. Moreover, the dimer-like topology of the plasmonic nanoantenna further enhances the nearfield, leading to an ultra-efficient trapping.

**Keywords**— Optical tweezers; Optical manipulation; Plasmonics; Integrated optics devices.

### I. INTRODUCTION

As firstly demonstrated in [1], focused laser beams can trap small particles released into liquid. The interaction between light and objects results in optical forces that arise from their momentum exchange. In general, the tweezing action depends on the electromagnetic nature of both the trap and the particle. To evaluate and quantify the tweezers performance, we can consider three linked quantities: the total force, the stiffness, and the potential energy.

The total force accounts for the contribution of two components, namely the scattering and the gradient force. In particular, the gradient force occurs when a displaceable object experiences a localized electromagnetic field. It is proportional to the cube of the particle radius  $r$  and to the gradient of the electric field modulus:

$$F_g \propto r^3 \nabla |E|^2.$$

The stiffness, representing the restoring action intensity of the trap, also gives an idea of both its efficiency and its spatial extent. The following expression holds for the stiffness calculated along the  $i$  direction:

$$k_i \propto r^3 \frac{d}{di} \nabla |E|^2.$$

The potential energy, which can be expressed as

$$U \propto r^3 |E_\omega|^2,$$

gives an idea of the trap stability. According to the Ashkin criterion [2], the potential energy well must be much deeper (at least 10 times) than the thermal energy  $k_B T$  of the system.

In order to ensure a stable trapping, in fact, it is imperative to compensate for the random kicks the particle receives in the presence of thermal agitation. It is worth pointing out that smaller particles are more difficult to trap since the gradient term depends on the cube of the particle radius. In order to compensate for the effect of the particle size, we can achieve stronger gradients by increasing the field localization.

Plasmonic structures are particularly efficient in concentrating the electromagnetic field in deep subwavelength volumes thanks to Surface Plasmon Polaritons (SPPs) and Localized Surface Plasmons (LSPs) at the interface between a dielectric material and Noble Metal Nanoparticles (NMPs). The excitation of the NMPs can be achieved by internal total reflection or, more effectively, by coupling the NMPs with a Silicon on Insulator (SOI) waveguide, as demonstrated by the authors in [3]-[5].

Here, we propose a plasmonic dimer configuration (i.e., nanoantenna) coupled to a silicon waveguide, which is capable of strongly enhancing the near field in the proximity of the dimer gap and, therefore, of achieving a stable trapping of subwavelength particles. In this contribution, we investigate the effect of the particle position, with respect to

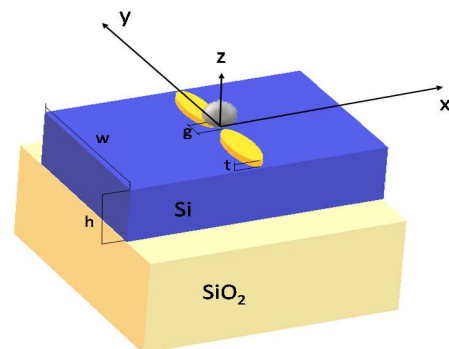


Figure 1. Scheme of the plasmonic gold dimer coupled to the SOI waveguide. A trapped particle is also represented (grey sphere).

the nanoantenna, on the trapping efficiency of dielectric and metallic nanoparticles dispersed in water.

In Section II, we report the results of the design and of the numerical simulations of plasmonic nano-tweezers, whereas, the conclusion is reported in Section III.

## II. INTEGRATED PLASMONIC NANO-TWEEZERS

The proposed plasmonic tweezers configuration is schematized in Figure 1. In particular, the considered dimer is constituted by two gold ellipsoidal nano-cylinders aligned along the  $y$ -axis and separated by a gap  $g=25$  nm. The geometrical sizes of each nano-cylinder are: radii  $r_x=30$  nm and  $r_y=90$  nm and thickness  $t=30$  nm. The particle to be trapped is also schematized as a sphere of radius  $r$ .

The dimer is coupled to a silicon waveguide having width  $w=500$  nm and height  $h=220$  nm. The geometrical sizes were optimized to achieve the optimal coupling between the Si waveguide and the dimer around the wavelength  $\lambda=1.55$   $\mu\text{m}$ .

We simulated the integrated dimer structure by three-dimensional Finite Difference Time Domain (FDTD) in presence of either a dielectric (polystyrene with refractive index  $n_p=1.59$ ) or a metallic (gold) spherical particle. The calculation of the total force  $F$  acting on the bead was performed from the total electromagnetic field, for a set of discrete positions of the bead. In all the simulations, we considered water as superstrate with refractive index  $n=1.33$ .

As an example, the numerical results obtained by the simulation of a polystyrene sphere immersed in water are reported in Figure 2. In particular, Figure 2 (a-c) show, respectively, the  $x$  component of the total force  $F_x$ , the  $x$  component of the stiffness  $k_x$ , and the  $z$  component of the total force  $F_z$ , as a function of the position  $x$  and of the wavelength  $\lambda$  when  $y=0$ . Similarly, Figure 2 (d-f) show  $F_y$ ,  $k_y$ , and  $F_z$  as a function of the position  $y$  and of the wavelength  $\lambda$ , when  $x=0$ .

In Figure 2 (d-f), where we consider a displacement of the particle along the  $y$  direction, we report the positions with positive values of  $y$  for the sake of reducing the computational time. Nonetheless, the behavior is symmetric with respect to the  $x$ -axis.

In Figure 2, the white solid lines correspond to the center of the dimer gap, the dotted blue lines denote the zeros of the stiffness and the solid green curves denote the equilibrium locus (i.e., the total force along  $x$  or  $y$  is zero). Since the corresponding stiffness is negative (see Figure 2(b)), along the green curve the object lies on a minimum of the potential energy, which also satisfies the Ashkin criterion for stable trapping as long as  $\lambda > 1.57$   $\mu\text{m}$ .

## III. CONCLUSION

The proposed dimer configuration is capable of efficiently trapping polystyrene nanoparticles in the middle of the dimer gap. Similar analyses were performed in the case of metallic nanoparticles, showing that the achieved optomechanical energy is one order of magnitude greater (in modulus) than in the case of dielectric particle trapping. Moreover, this effect is associated with a significant variation of the SOI waveguide transmittance, thus allowing the detection and the monitoring of the particle-trapping event.

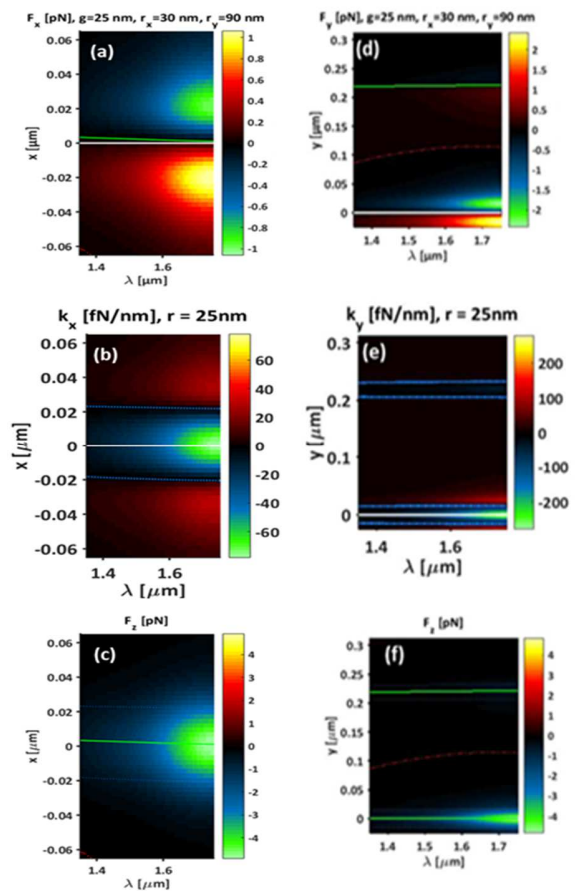


Figure 2. (a) Total force  $F_x$ , (b) stiffness  $k_x$ , and (c) total force  $F_z$  as a function of the position  $x$  and of the wavelength  $\lambda$ , and (d) Total force  $F_y$ , (e) stiffness  $k_y$ , and (f) total force  $F_z$  as a function of the position  $y$  and of the wavelength  $\lambda$ , for a polystyrene sphere of radius  $r=25$  nm.

## ACKNOWLEDGMENT

The research was conducted in the framework of the project Galileo 2018 G18-625/PHC Galilée 39622NL.

## REFERENCES

- [1] A. Ashkin, "Acceleration and Trapping of Particles by Radiation Pressure", *Phys. Rev. Lett.*, vol. 24, pp. 156-159, 1970.
- [2] A. Ashkin, J. M. Dziedzic, J. E. Bjorkholm, and S. Chu, "Observation of a single-beam gradient force optical trap for dielectric particles", *Opt. Lett.*, vol. 11, pp. 288-290, (1986).
- [3] G. Magno et al., "Integrated plasmonic nanotweezers for nanoparticle manipulation," *Opt. Lett.*, vol. 41(16), pp. 3679-3682, 2016.
- [4] A. Ecarnot, G. Magno, V. Yam, and B. Dagens, "Ultra-efficient nanoparticle trapping by integrated plasmonic dimers," *Opt. Lett.*, vol. 43(3), pp. 455-458, 2018.
- [5] G. Magno et al., "Strong coupling and vortexes assisted slow light in plasmonic chain-SOI waveguide systems", *Scientific Reports*, vol. 7, pp. 7228, 2017.

# Differential Optical Sensing through Coupled Micro Ring Resonators

Ali Emre Kaplan, Geatano Bellanca

Department of Engineering  
 University of Ferrara  
 Ferrara, Italy  
 e-mails: aliemre.kaplan@unife.it,  
 gaetano.bellanca@unife.it

Paolo Bassi

Department of Electrical, Electronic  
 and Information Engineering  
 University of Bologna  
 Bologna, Italy  
 e-mail: paolo.bassi@unibo.it,

**Abstract**—We theoretically investigate the performance of a double micro ring resonator for integrated optical sensing applications. The transmission characteristics of the proposed device can be driven in two distinct operations by controlling the difference of the round-trip phase shifts of the coupled resonators. The enhancement of the limit of detection by a factor of 5.6 compared to a single micro ring based sensor is demonstrated. Beside the fact that the single and double ring based schemes have the same spectral wavelength sensitivity of 918 nm per refractive index unit, the latter scheme also supports the intensity interrogation which can be used for on-chip thermal noise compensation via integrated micro heaters.

**Keywords**—Micro ring resonators; Optical sensing; Integrated photonic circuits.

## I. INTRODUCTION

Integration of microfluidics with Photonic Integrated Circuits (PIC) promotes new emerging biosensing technologies. Especially Silicon based on-chip sensors draw an intense interest thanks to their compactness, cost effectiveness and Complementary Metal-Oxide Semiconductor (CMOS) compatible properties. So far, various types of on-chip Si PICs, such as Micro Ring Resonator (MRR), Mach-Zehnder interferometer, photonic crystal and Bragg grating have been investigated for label-free detection [1] and, among them, MRR based sensors provide higher sensitivity and denser integration [2]. A comprehensive review paper about Silicon MRR based biosensors can be found in [3]. The add-drop configuration of MRR allows a sensing application that measures the resonance wavelength shift according to up cladding index change induced by microfluids [4]. Figure 1 illustrates a typical working principle of a ring based sensing scheme. A suitable measurement setup for such devices consists of a tunable laser source that provides the incoming light and a spectrometer to measure the spectral shift of resonance wavelengths after binding.

The characterization wavelength interrogation is based on the extraction of refractive index change information via resonant wavelength shifts induced by the interaction of fluids and the evanescent field of a resonant cavity. The resonance wavelength of a single ring is defined as

$$m \cdot \lambda_{res} = n_{eff} L \quad (1)$$

where  $L$  is the circumference of the ring,  $n_{eff}$  is the effective refractive index of the resonant mode and  $m$  is an integer, and a modification of  $n_{eff}$  results in a variation of  $\lambda_{res}$ . The amount of the wavelength shift depends on how much flowing analyte alters the effective refractive index and it can

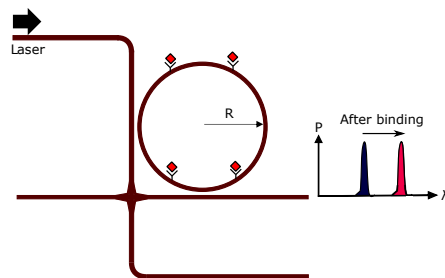


Figure 1. Schematic of a conventional micro ring resonator based biosensor.

be formulated as [5]

$$\Delta\lambda = \frac{\Delta n_{clad} \lambda_{res}}{n_g} \quad (2)$$

where  $n_g$  is the group index of the guided mode and  $\Delta n_{clad}$  is the refractive index change of the cladding induced by the interaction of the fluids and the ring resonator. This interaction can occur either by analyte binding or concentration change of substances and the types of sensing are then called label-free and bulk sensing, respectively. The MRR with high quality factor, or Q-factor, is desirable for enhanced detection limit of sensing applications. However, environmental and microfluidics induced thermal perturbations must be considered since such spurious effects may significantly affect the spectral wavelength shift at higher Q-factor. Previously, a sensing scheme based on cascaded MRRs has been investigated using shared flow channel above the reference and sensing rings where two solutions flow independently [6]. However, it was found difficult to control precisely the temperature and pressure of each solution. Another approach uses two frequency locked laser sources for imprinting the temperature difference of the rings in radio-frequency domain and achieves the state of the art sensitivity in the order of  $10^{-8}$  RIU (Refractive Index Unit) [7] but still this method suffers from lack of thermal equilibrium of the sensor and requires more than one laser source. The previously reported differential sensing platforms with thermal compensation perform only wavelength interrogation. Here, we propose an alternative scheme based on a double ring structure that is able to also support the intensity interrogation that can help to eliminate the need of external thermal stabilization systems and a reference fluid flow. In Figure 2, the working principle of the proposed device

is illustrated. Two micro rings with the radius  $R_1$  and  $R_2$  are indirectly coupled via a central bus waveguide. When the two rings are synchronized ( $\theta_1 = \theta_2$ ), both resonators share the same resonance wavelength and thanks to the common light path, which is the vertical waveguide section, the switched wavelength propagates back to the input port, as shown in Figure 2a. In this case, the through port in the middle and the upper and bottom drop ports have transmission dips. In the second operational regime, each ring switches its own resonance wavelengths to the upper and bottom drop ports, as a result of different round-trip phase shifts ( $\theta_1 \neq \theta_2$ ). The through port has, therefore, two transmission dips where the resonances appear and the transmitted powers at the drop ports increase (see Figure 2b). The phase shift difference of the two paths can be determined by different radius of the two rings or by effective index detuning of the one of two ring waveguides through, e.g., thermo-optic effect, if the resonators have equal radii.

In our theoretical work, we assume that the rings are identical and the induced effective index change occurs in one of the rings, while the other ring is being used as the reference one. Since the overall output transmissions depend only on the phase difference, we refer to this scheme as a differential sensing scheme.

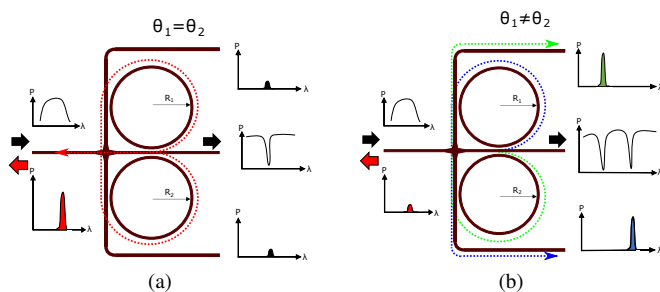


Figure 2. Working principle of the coupled ring sensing scheme: synchronous phase shift (a) and asynchronous (b) after binding.

In this work, we will theoretically discuss the performance of the proposed sensing scheme in terms of sensitivity, Limit of Detection (LOD) and thermal compensation by comparing the proposed configuration to the conventional single ring results analyzed using the same design parameters, such as coupling strength of the vertical and horizontal coupling sections, waveguide geometry and radius. The paper is organized as follows. In Section 2, we introduce sensor parameters, sensitivity and limit of detection. Also, we show the effect of phase synchronization on the transmission behavior of the sensor. Section 3 provides the results of both wavelength and intensity interrogations and compare the results of the differential sensing to those obtained from the single ring configuration. Finally, we discuss the better performance attained by using differential sensing for practical issues, such as the sensor calibration and thermal compensation.

## II. TRANSMISSION CHARACTERISTICS OF THE PROPOSED SENSING SCHEME

We analytically study both structures based on the Transfer Matrix Method obtained from coupling relationships of the resonators in the two port and three port coupler sections [8]–[10]. The design parameters such as radii of the rings

and coupling ratios of the horizontal and vertical couplers are inserted in the transfer matrices. The effective refractive index  $n_{eff}$  of the Transverse Electric (TE) mode propagating of the Silicon-On-Insulator (SOI) waveguide (480x220 nm), are obtained through the Finite Element Method (FEM) simulations [11]. In our scenario, the bottom ring is considered as a reference and its round trip phase shift ( $\theta_2$ ) can be detuned by, for example, micro integrated heaters. Instead, the phase shift of the upper sensor ring ( $\theta_1$ ) changes due to the presence of the specimen. Assuming that  $R_1 = R_2$ , then round trip phase shifts for sensor and reference rings are defined as  $\theta_1 = n_{eff1} \cdot L$  and  $\theta_2 = n_{eff2} \cdot L$ , respectively. A special case occurs when the rings have the same phase shift as shown in Figure 3a. The reflected wavelength reaches its maximum near critical coupling where a high extinction ratio is present for the through port along with weak drop port transmissions. When the effective index of the sensor ring is changed due to the binding of analytes on the cladding, the reference signal (green curve) remains at the same wavelength, while the sensing wavelength (blue curve) experiences red shift, as shown in Figure 3b. In addition, the reflection power decreases dramatically.

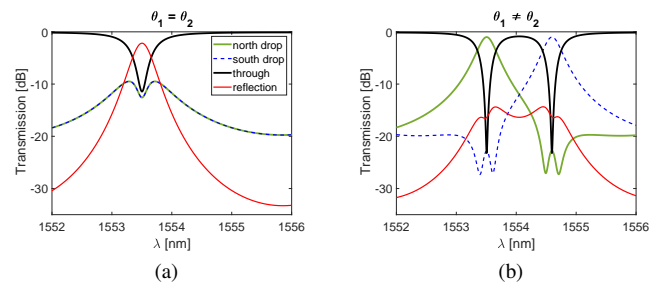


Figure 3. Transmitted powers of through port (black), upper and bottom drop ports (green and blue) and back reflection (red) in initial condition (a) and sensing operation (b).

In order to evaluate pros and cons of the presented device over the single ring scenario, we first need to calculate its sensitivity using the following description [3]:

$$S = \frac{\Delta\lambda}{\Delta n_{clad}} \quad (3)$$

As we analyze the device theoretically, it is convenient to use the  $\Delta n_{eff}$  instead of the  $\Delta n_{clad}$  because the rings are identical in both single and double ring schemes. The minimum detectable change of the  $n_{eff}$  determines the *LOD* which corresponds also to the minimum wavelength shift  $\Delta\lambda$ . Since this sensing scheme requires a spectrum analysis, minimum detection depends on the setup. To eliminate setup dependency of the measurements, an intrinsic *iLOD* can be defined as [3]:

$$iLOD = \frac{FWHM}{S} \quad (4)$$

meaning that the Full Width Half Maximum (FWHM) of the resonance peak is the lower limit of the wavelength shift needed to distinguish two successive wavelengths.  $S$  and *iLOD* are used as the test parameters to investigate the performance of the device.

### III. PERFORMANCE COMPARISON OF SINGLE AND COUPLED DOUBLE RING SENSORS

An example of wavelength shifting at the drop ports obtained from  $n_{eff}$  detuning is illustrated in Fig 4. Both rings have the same radius of  $20\mu m$  and the coupling ratio is fixed at  $K = 0.1$  for both single and double ring configurations. The green curves and the blue curves in Figure 4a represent reference and sensing signals of the double ring sensor, respectively. In the double ring scheme, the sensing signal exhibits a red-shift and an intensity increase, while the reference signal intensity increases by maintaining the fixed wavelength. On the other hand, the single ring sensor (see Figure 4b) has only wavelength shift with negligible peak intensity variations. Thus, the double ring configuration also allows to analyze intensity interrogation in addition to wavelength interrogation.

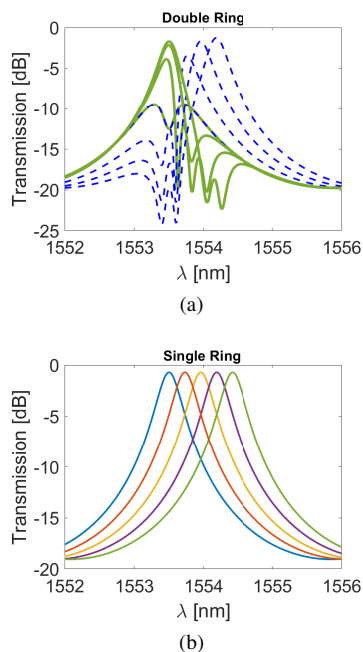


Figure 4. Wavelength shifts induced by the change effective refractive index of the drop ports of the double ring (a) and the single ring (b) configurations.

The comparison of the two schemes is shown in Figure 5. According to the  $\Delta n_{eff}$ , the wavelength shifts  $\Delta\lambda$  (red lines) linearly increase in both devices. However, the peak intensity variation  $\Delta P$  (blue curves) is available only for the double ring sensor and it shows a rapid increase for a small range of  $\Delta n_{eff}$ , as shown in Figure 5a. On the contrary, the single ring sensor has a very small change in peak intensities so the  $\Delta P$  remains almost constant, as shown in Figure 5b. Table I summarizes the calculated sensing parameters. The wavelength shift sensitivity  $S_{\Delta\lambda}$  nm/RIU (RIU:Refractive Index Unit) is calculated from the slopes of the  $\Delta\lambda$  and, since both devices have identical rings,  $S_{\Delta\lambda}$  is found to be the same (918 nm/RIU). As opposed to the single ring case, the minimum resonance intensity sensitivity of 515 dB/RIU within the range  $\Delta n_{eff} = 0.001$  of the double ring sensor demonstrates that it is possible to achieve intensity interrogation for very accurate sensing performance in a small  $\Delta n_{eff}$  span. The  $S_{\Delta P}$  increases as the index change span decreases. The most significant difference of the sensors appears for the limit of detection. The resonance line width determines the  $iLOD$

such that it ensures at least 3 dB bandwidth separation of two successive resonances. We found that the coupled double ring sensor requires smaller effective refractive index change to meet  $iLOD$  condition than single ring does and the detection limit of the double ring is found to be enhanced by a factor of 5.6 at the price of increased insertion loss of the sensor.

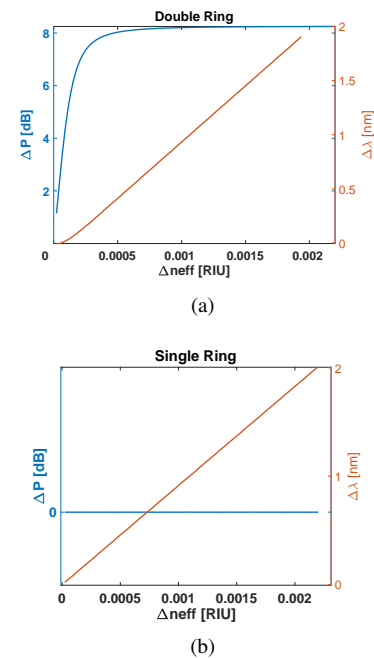


Figure 5. Comparison of  $\Delta P$  (blue curve) and  $\Delta\lambda$  (red curve) with respect to the induced  $\Delta n_{eff}$  for coupled double ring (a) and single ring (b) sensing schemes.

TABLE I. CALCULATED SENSOR PARAMETERS: SENSITIVITIES FOR WAVELENGTH  $S_{\Delta\lambda}$  AND INTENSITY  $S_{\Delta P}$  INTERROGATIONS AND DETECTION LIMITS.

	$S_{\Delta\lambda}$ [nm/RIU]	$S_{\Delta P}$ [dB/RIU]	$iLOD$ [RIU]
Single Ring	918	0.6	$2.47 \cdot 10^{-4}$
Double Ring	918	515	$0.44 \cdot 10^{-4}$

The limiting factor for the intensity sensing is based on the convergence of the  $\Delta P$  curve. For instance, when  $\Delta n_{eff}$  is equivalent to around 0.8 nm wavelength shift, the change in the transmitted power becomes negligible. This effect can be noticed from Figure 4a where the green curves around the maximum transmission are very close to each other. However, minimum detectable intensity change is limited by the power measurement accuracy. The curve of  $\Delta P$  shown in Figure 5a can give different values of  $S_{\Delta P}$  depending on the minimum acceptable intensity interval; we fixed such value at 0.1 dB and considered that changes below this value are negligible. Therefore, the reported  $S_{\Delta P}$  in Table I is the minimum sensitivity. The maximum intensity sensitivity can be achieved in smallest  $\Delta n_{eff}$  such that the power of peaks increases very rapidly and reaches very high sensitivity up to  $4.5 \cdot 10^4$  dB/RIU within the value of  $iLOD$ . Furthermore, it is possible to enhance the intensity interrogation range by increasing the coupling ratio, as shown in Figure 6. Stronger coupling strength gives rise to smoother transitions over the x-axes. But,

as a consequence of an increased coupling ratio, the FWHM rises and results in *i*LOD impairment.

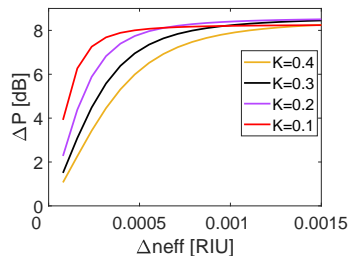


Figure 6. Effect of coupling ratio increments on the range of detectable  $\Delta n_{eff}$  in the intensity interrogation scheme.

One of the main noise sources for biosensors is thermal noise. Either environmental or resonator based self-induced thermal noise becomes critical for very highly sensitive sensors, hence the temperature of the sensor should be precisely controlled during the measurement. This adds another difficulty to realize reliable sensors. To overcome this issue, the proposed differential sensing scheme based on the coupled resonators can in fact provide an alternative approach to compensate thermal noise effects by an initial calibration of the reference ring phase shift by searching the local maximum of reflection that guarantees single resonance wavelength. Once two coupled rings are synchronized, which implies  $\theta_1 = \theta_2$ , then the resulting  $S_{\Delta\lambda}$  and  $S_{\Delta P}$  can be disposed of the thermal noise. During the sensing process, it is possible to retrieve spurious wavelength shift by monitoring the reference resonance wavelength. The amount of wavelength shift gives the portion of resonance shift of the sensing wavelength caused by thermal noises.

#### IV. CONCLUSION

We proposed and theoretically studied a novel optical biosensing scheme based on differential sensing through the coupled micro ring resonators in SOI technology. The assessment of the sensitivity and limit of detection of the proposed device is done by comparing the results obtained from the conventional single ring sensor, having the same technology design parameters such as coupling ratio and radius. Sensitivity of the wavelength interrogation is found to be identical for each type of device, while the double ring sensor has enhanced limit of detection by a factor of 5.6 compared to the single ring sensor.

In addition, the presented device also supports intensity interrogation which is not the case for single ring if only the spectral measurement is considered. However, spectral interrogation is found to be possible only for a very small effective refractive index change. The way of increasing the range of a detectable index change is reported and possible resulting impairment on the limit of detection is described.

Thanks to the possibility of an initial calibration of the device by monitoring the back reflection, differential sensing scheme can eliminate environmental and self-induced thermal noises. Therefore, this scheme can provide on-chip thermal control by integrated micro resistors on the reference ring for realizing reliable integrated biosensors and cost effective measurements.

#### REFERENCES

- [1] E. Luan, H. Shoman, D. M. Ratner, K. C. Cheung, and L. Chrostowski, "Silicon photonic biosensors using label-free detection," *Sensors*, vol. 18, no. 10, 3519, 2018. [Online]. Available: <https://www.mdpi.com/1424-8220/18/10/3519> [retrieved: September, 2019].
- [2] G. A. Rodriguez, S. Hu, and S. M. Weiss, "Porous silicon ring resonator for compact, high sensitivity biosensing applications," *Opt. Express*, vol. 23, no. 6, 2015, pp. 7111–7119.
- [3] P. Steglich, M. Hülsemann, B. Dietzel, and A. Mai, "Optical biosensors based on silicon-on-insulator ring resonators: A review," *Molecules*, vol. 24, no. 3, 519, 2019. [Online]. Available: <https://www.mdpi.com/1420-3049/24/3/519> [retrieved: September, 2019].
- [4] T. Taniguchi *et al.*, "Detection of antibody-antigen reaction by silicon nitride slot-ring biosensors using protein g," *Optics Communications*, vol. 365, 2016, pp. 16 – 23.
- [5] T. Claes *et al.*, "Label-free biosensing with a slot-waveguide-based ring resonator in silicon on insulator," *IEEE Photonics Journal*, vol. 1, no. 3, Sep. 2009, pp. 197–204.
- [6] D. Kim *et al.*, "On-chip integrated differential optical microring refractive index sensing platform based on a laminar flow scheme," *Opt. Lett.*, vol. 40, no. 17, Sep 2015, pp. 4106–4109.
- [7] L. Stern *et al.*, "Ultra-precise optical to radio frequency based chip-scale refractive index and temperature sensor," *Optica*, vol. 4, no. 1, Jan 2017, pp. 1–7.
- [8] Chang-Min Kim and Young-Joon Im, "Switching operations of three-waveguide optical switches," *IEEE Journal of Selected Topics in Quantum Electronics*, vol. 6, no. 1, 2000, pp. 170–174.
- [9] H. Kogelnik and R. Schmidt, "Switched directional couplers with alternating  $\Delta\beta$ ," *IEEE Journal of Quantum Electronics*, vol. 12, no. 7, 1976, pp. 396 – 401.
- [10] A. Yariv, "Universal relations for coupling of optical power between microresonators and dielectric waveguides," *Electronics Letters*, vol. 36, no. 4, 2000, pp. 321–322.
- [11] COMSOL Multiphysics, <https://www.comsol.com> [retrieved: September, 2019].

# True Random Number Generation with Beam Splitters under Combined Input Scenarios using Defined Quantum States to Increase the Security of Cryptographic Devices

Martin Suda

Gerald Dißauer

Florian Prawits

Austrian Institute of Technology  
(AIT)  
Vienna, Austria

Secure Information Technology Center  
Austria (A-SIT)  
Vienna, Austria

Austrian Institute of Technology  
(AIT)  
Vienna, Austria

Email: martin.suda@ait.ac.at   Email: gerald.dissauer@a-sit.at   Email: florian.prawits@ait.ac.at

**Abstract**—Cryptographic devices, e.g., Hardware Security Modules (HSMs) are crucial to the trustworthiness of computer applications that provide critical services such as digital signature systems. Random numbers are used to strengthen the security of HSMs. Due to the problem of deterministic and thus predictable random sources and the complexity to derive true coincidence with computer systems, quantum mechanical effects can be exploited to derive perfect randomness. In this paper, we present an approach to increase the security of HSMs by using 50:50 splitters under combined input scenarios to derive true random numbers based on quantum mechanics.

**Keywords**—Beam Splitter; Cryptography; Quantum Mechanics; Quantum Random Number Generation; Quantum States; Hardware Security Module; HSM; True Randomness.

## I. INTRODUCTION

1) *Motivation*: According to our conducted research in quantum optics, the generation of quantum random numbers with Beam Splitters (BS) relying on the physical effects of light quanta is particularly underdeveloped in terms of practical applications. Such practical applications include the computation of random numbers for cryptographic protocols and Hardware Security Modules (HSMs) [1]. HSMs that rely on cryptographic protocols to engineer secure systems [2] can be used to derive cryptographic key material and store private data or master keys [3] in protected hardware devices, e.g., PCI (Peripheral Component Interconnect) devices that are optimized for cryptographic operations [4]. Therefore, such cryptographic devices are integrated into complex practical applications, e.g., to create qualified electronic signatures [5] which means that electronic documents are signed digitally. Such documents are legally valid, for instance. Other industrial applications are implemented in data centers [3] and particularly in the banking sector [1] (e.g., for mobile payment solutions) where the key management for database encryption solutions [6] are installed.

2) *Problem statement*: HSMs for the above mentioned industrial applications are often certified against either (1) FIPS (Federal Information Processing Standard) 140-2 [7] (newer Version: FIPS 140-3 [8]) or (2) Common Criteria [9]–[11], e.g., EAL4+ (Evaluation Assurance Level) [11] which was also codified in the ISO/IEC (International Organization for Standardization / International Electrotechnical Commission) 15408 standard [12]–[14]. Such certifications of software-intensive products are used to validate the realized security

functions (e.g., SFR - Security Functional Requirements of the Common Criteria) [10] and moreover to assure (SAR - Security Assurance Requirements of the Common Criteria) [11] the compliance of the selected product against the claimed security functions. That means that a particular minimum-level of security (e.g., EAL4+) for those integrated devices is assured.

Such certifications often require Deterministic Random Bit Generators (DRBGs) in accordance with NIST (National Institute of Standards and Technology) SP (Special Publication) 800-90A [15] or alternatively demand pseudo-random data (seed) as inputs to obtain random numbers. Feasible sources to derive seeds are the 1) system clock [10], 2) system registers [10], 3) date [10], 4) time [10], or 5) external events [15] but the aforementioned computational sources do not provide true randomness [16], unfortunately.

However, the use of true sources of randomness (i.e., True Random Number Generators - TRNGs) are increasingly required to seed deterministic random number generators and thus to increase the entropy [7][15]. Alternatively, physical sources can be used to obtain real random numbers (e.g., deriving it from noise) rather than by means of deterministic algorithms. As a result, developers must demonstrate that their used entropy sources provide a sufficient level of randomness.

Industrially relevant examples of such practical applications include 1) to increase the security of cryptographic protocols, or 2) to strengthen the device-internal cryptographic materialmanagement (e.g., for FIPS 140-2 or FIPS 140-3) of HSMs under real circumstances. Such HSMs derive random numbers from predictable algorithms and therefore those obtained random numbers do not rely on real coincidence.

In contrast, quantum random numbers are obtained from the fundamental principles of quantum mechanics which means that such random numbers are derived from the perfect randomness of quantum mechanical effects [17]. Therefore, such random number generators produce random data that are unpredictable. Quantum random number generators have been recently tested for 71-day non-stop long-term applications [18].

3) *Our proposed solution*: To overcome the limitations of imperfect random numbers in terms of cryptographic devices, we propose a solution to generate quantum mechanical random numbers that are derived from several input configurations under defined scenarios for 50:50 Beam Splitters. In order to assess reasonable input configurations to obtain practically

applicable random data outputs, we consider the following input configurations ( $\hat{a}_0$  and  $\hat{a}_1$ , Figure 1) for our BS:

- $|0\rangle$  and  $|1\rangle$  (quantum vacuum state on  $\hat{a}_0$  and single-photon on  $\hat{a}_1$ )
- $|1\rangle$  and  $|1\rangle$
- $|0\rangle$  and  $|\alpha\rangle$  (coherent state on  $\hat{a}_1$ )
- $|\alpha\rangle$  and  $|\beta\rangle$  (two Weak Coherent States - WCS)
- $|0\rangle$  and  $(|0\rangle + |1\rangle)$  (superposition on  $\hat{a}_1$ )
- $(|0\rangle + |1\rangle)$  and  $|1\rangle$
- $|1\rangle$  and  $|\alpha\rangle$
- $\frac{1}{\sqrt{N}}(|\alpha\rangle|\beta\rangle + |\beta\rangle|\alpha\rangle)$  (Entangled Coherent State - ECS)
- $|\beta\rangle$  and  $\frac{1}{\sqrt{N}}(|\beta\rangle + |-\beta\rangle)$  (Coherent Superposition State - CSS)

We, therefore, get random outputs behind the BS under the above mentioned defined input scenarios.

4) *The benefit:* Quantum random number generators [16], which derive real randomness with BS under defined input scenarios, can be used as physical sources to obtain perfect random numbers. As a result, it is possible to increase the security of HSMs and particularly the randomness of the key material inside of the HSM or of cryptographic protocols. That means that we are able to overcome the limitations of predictable random sources for current solutions because the underlying randomness is based on the intrinsic effects of true randomness derived from quantum mechanics.

This paper is organized as follows. After the introduction in Section I (see above), we discuss the BS (cf., II-A) and present 9 examples (cf., II-B) for the aforementioned input and related output states in Section II. Section III concludes our paper.

## II. BS AND EXAMPLES

### A. Beam Splitter

Below, we describe the Beam Splitter - a semi-permeable mirror - quantum mechanically. To obtain true randomness, we choose a semi-permeable BS where the incident light is transmitted with a 50% probability and thus 50% of the incident light is reflected (denoted by 50:50). Alternatively, one can choose arbitrary configurations of the BS. However, only the 50:50 configuration derives true randomness [19]. Such a device is constructed so that it has 2 input modes ( $\hat{a}_0$ ,  $\hat{a}_1$ ) and 2 output modes ( $\hat{a}_2$ ,  $\hat{a}_3$ ) (Figure 1).

The quantum mechanics of BS can be found in [20]–[24]. The most important relation is given by Heisenberg's uncertainty relation:

$$[\hat{a}_i, \hat{a}_j^+] = \delta_{ij}, \quad \hat{a}^+ \hat{a} = \hat{n}, \quad \hat{a} \hat{a}^+ = 1 + \hat{n}. \quad (1)$$

$\hat{a}^+$  is the creation operator and  $\hat{a}$  the annihilation operator for photons.  $\hat{n}$  is called particle operator. The matrix equation for a BS can be written as

$$\begin{pmatrix} \hat{a}_2 \\ \hat{a}_3 \end{pmatrix} = \frac{1}{\sqrt{2}} \begin{pmatrix} 1 & i \\ i & 1 \end{pmatrix} \begin{pmatrix} \hat{a}_0 \\ \hat{a}_1 \end{pmatrix} = \hat{T} \begin{pmatrix} \hat{a}_0 \\ \hat{a}_1 \end{pmatrix}. \quad (2)$$

$\hat{T}$  is a unitary matrix where  $\hat{T} \hat{T}^+ = \mathbb{1}$  holds. For a 50 : 50 BS the following relations can be deduced (we choose, e.g., phase  $i = \exp(i\pi/2)$  for reflection:  $\hat{a}_2 = t\hat{a}_0 + r\hat{a}_1$  and  $\hat{a}_3 = r\hat{a}_0 + t\hat{a}_1$ ):

$$\begin{aligned} \hat{a}_2^+ &= \frac{1}{\sqrt{2}}(\hat{a}_0^+ - i\hat{a}_1^+), \quad \hat{a}_3^+ = \frac{1}{\sqrt{2}}(-i\hat{a}_0^+ + \hat{a}_1^+) \rightarrow \\ \hat{a}_0^+ &= \frac{1}{\sqrt{2}}(\hat{a}_2^+ + i\hat{a}_3^+), \quad \hat{a}_1^+ = \frac{1}{\sqrt{2}}(i\hat{a}_2^+ + \hat{a}_3^+). \end{aligned} \quad (3)$$

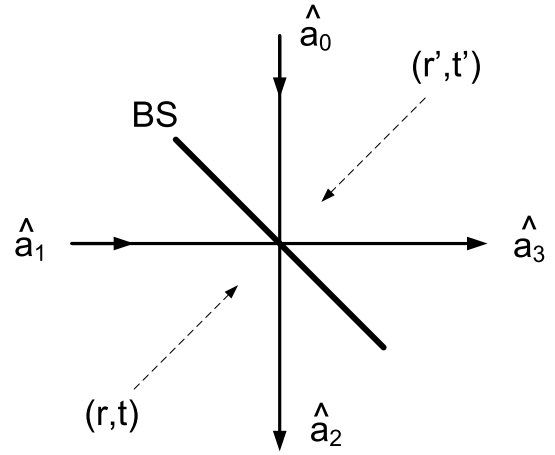


Figure 1. BS: Quantum mechanical description,  $r$  and  $t$  are reflection and transmission coefficients, respectively; see text. In principle  $r$  and  $t$  can be different for the front and back of the BS.

The examples below are given in order to demonstrate the mode of operation of a BS with genuine quantum input states and output states which are appropriate for Quantum Random Numbers (QRN) [16]. Such output states have the following structure:  $(|n\rangle_2|0\rangle_3 + |0\rangle_2|n\rangle_3)$  or  $(|\alpha\rangle_2|0\rangle_3 + |0\rangle_2|\alpha\rangle_3)$  where  $|n\rangle$  are Fock states and  $|\alpha\rangle$  are coherent states which are each entangled to the vacuum  $|0\rangle$ . Hence, coincidences must not appear in the output modes.

### B. Examples

1) *One Photon in input 1:*  $|0\rangle_0|1\rangle_1$ : Now, in this first example the input state is  $|0\rangle_0|1\rangle_1 = \hat{a}_1^+|0\rangle_0|0\rangle_1$ . We recall that in quantum optics (e.g., [20]) a photon can be created from vacuum by means of the creation operator:  $\hat{a}^+|0\rangle = |1\rangle$ . Generally, for  $n$  photons,  $\hat{a}^+|n\rangle = \sqrt{n+1}|n+1\rangle$  and  $\hat{a}|n\rangle = \sqrt{n}|n-1\rangle$  holds.  $|n\rangle$  are the Fock states of light.

Experimentally, a single photon state (denoted by  $|1\rangle$ ) can be generated by Parametric Down-Conversion (PDC) using non-linear crystals. That means that two photons are created simultaneously, where one of those photons is used for the BS-experiment. The other one is registered in terms of synchronization purposes of the created photon pair. It is important to note that the process of PDC occurs with low probability s.t. random numbers generated by this means will show low yield [20]–[24]. To overcome this limitation, weak coherent states are able to be used for the generation of approximately single photon states (cf., case 2 below).

Using (3), one gets behind the BS:

$$\begin{aligned} |0\rangle_0|1\rangle_1 &\xrightarrow{BS} \frac{1}{\sqrt{2}}(i\hat{a}_2^+ + \hat{a}_3^+)|0\rangle_2|0\rangle_3 = \\ &= \frac{1}{\sqrt{2}}(i|1\rangle_2|0\rangle_3 + |0\rangle_2|1\rangle_3). \end{aligned} \quad (4)$$

This is an important result of a balanced BS. It means that a single input photon in mode 1 together with a vacuum input in mode 0 is equally transmitted and reflected with probability  $\frac{1}{2}$ . An important method of generating quantum random numbers [16] relies on this method. This result is exactly what is expected. It explains also that there are no coincidences. If one measures the photon in output port 2(3)

no photon is measured in output 3(2). One can say as well that the photon is entangled with the vacuum behind the BS. Conversely one can say: If there are in fact no coincidences, then we have a genuine single photon source. Obviously, the BS is a "passive" element which neither creates nor annihilates photons.

The density operator  $\hat{\rho}_{23}$  of the output states behind the BS is:

$$\begin{aligned}\hat{\rho}_{23} &= \frac{1}{2}(|1\rangle_2|0\rangle_3 + |0\rangle_2|1\rangle_3)(-i\langle 2|_3\langle 0| + \langle 2|_3\langle 1|) = \\ &= \frac{1}{2}\{|1\rangle_2|0\rangle_3 \langle 2|_3\langle 0| + |0\rangle_2|1\rangle_3 \langle 2|_3\langle 1| + \\ &+ |1\rangle_2|0\rangle_3 \langle 2|_3\langle 1| - i|0\rangle_2|1\rangle_3 \langle 2|_3\langle 0|\}.\end{aligned}\quad (5)$$

This density operator contains the full information of coherence. It includes all off-diagonal elements. If only one output is measured (e.g., output 2) one has to apply the partial trace over output 3:

$$\begin{aligned}\hat{\rho}_2 = Tr_3\hat{\rho}_{23} &= \sum_{n=0}^{\infty} \langle n|_3\hat{\rho}_{23}|n\rangle_3 = \\ &= \frac{1}{2}(|0\rangle_2 \langle 2|_3\langle 0| + |1\rangle_2 \langle 2|_3\langle 1|)\end{aligned}\quad (6)$$

and analog  $\hat{\rho}_3 = \frac{1}{2}(|0\rangle_3 \langle 3|_3\langle 0| + |1\rangle_3 \langle 3|_3\langle 1|)$ . Equation (6) describes a statistical mixture. After performing the measurement, no off-diagonal terms exist, which would imply coherence. The output states appear with 50% probability each and there are no coincidences. Measuring the particle number for output 2, one keeps the following result:  $\bar{n}_2 = Tr_2(\hat{\rho}_2\hat{n}_2) = \frac{1}{2}(\langle 2|_3\langle 0|_3\hat{n}_2|0\rangle_3 + \langle 2|_3\langle 1|_3\hat{n}_2|1\rangle_3) = \frac{1}{2}(0 + 1) = \frac{1}{2}$ . This result signifies the mean particle number in output 2. Similar results are obtained for output 3.

2) *Coherent state  $|\alpha\rangle$  in input 1:*  $|0\rangle_0|\alpha\rangle_1$ : The coherent state [20]–[24]

$$\begin{aligned}|\alpha\rangle &= e^{-|\alpha|^2/2} \sum_{n=0}^{\infty} \frac{\alpha^n}{\sqrt{n!}} |n\rangle \\ &= e^{-|\alpha|^2/2} [ |0\rangle + \alpha|1\rangle + \frac{\alpha^2}{\sqrt{2}}|2\rangle + \dots ]\end{aligned}\quad (7)$$

is similar to a classical state. Depending on  $|\alpha|^2$  (which represents the mean number of photons), a coherent state can contain a high number of photons. Hence, it is rather contrary to the highly non-classical single-photon state considered in the first example. Experimentally, a coherent state can be created by a laser beam.  $\alpha$  is a complex number and  $|\alpha|^2$  is the mean photon number. Coherent states are solutions of the eigen-value equation  $\hat{a}|\alpha\rangle = \alpha|\alpha\rangle$ . The displacement operator  $\hat{D}(\alpha) = e^{\alpha\hat{a}^\dagger - \alpha^*\hat{a}}$  applied on a vacuum state  $|0\rangle$  is able to generate a coherent state  $|\alpha\rangle$ :  $\hat{D}(\alpha)|0\rangle = |\alpha\rangle$ . In our example, we have in input mode 1 a coherent state and in input mode 0 a vacuum state:  $|0\rangle_0|\alpha\rangle_1 = \hat{D}_1(\alpha)|0\rangle_0|0\rangle_1$ . Using (3), one

obtains:

$$\begin{aligned}|0\rangle_0|\alpha\rangle_1 &\xrightarrow{BS} e^{\frac{\alpha}{\sqrt{2}}(\hat{a}_2^\dagger + \hat{a}_3^\dagger) - \frac{\alpha^*}{\sqrt{2}}(-i\hat{a}_2 + \hat{a}_3)} |0\rangle_2|0\rangle_3 = \\ &= e^{(\frac{i\alpha}{\sqrt{2}})\hat{a}_2^\dagger - (\frac{i\alpha}{\sqrt{2}})^*\hat{a}_2} \times \\ &\quad \times e^{(\frac{\alpha}{\sqrt{2}})\hat{a}_3^\dagger - (\frac{\alpha}{\sqrt{2}})^*\hat{a}_3} |0\rangle_2|0\rangle_3 = \\ &= \hat{D}_2\left(\frac{i\alpha}{\sqrt{2}}\right)\hat{D}_3\left(\frac{\alpha}{\sqrt{2}}\right)|0\rangle_2|0\rangle_3 = \\ &= \left|\frac{i\alpha}{\sqrt{2}}\right\rangle_2 \left|\frac{\alpha}{\sqrt{2}}\right\rangle_3\end{aligned}\quad (8)$$

The appropriate density operators are:

$$\begin{aligned}\hat{\rho}_{23} &= \left|\frac{i\alpha}{\sqrt{2}}\right\rangle_2 \left|\frac{\alpha}{\sqrt{2}}\right\rangle_3 \langle 2|_3 \langle \frac{\alpha}{\sqrt{2}}| \\ \hat{\rho}_2 &= Tr_3(\hat{\rho}_{23}) = \\ &= \left|\frac{i\alpha}{\sqrt{2}}\right\rangle_2 \langle 2|_3 \langle \frac{i\alpha}{\sqrt{2}}|\end{aligned}\quad (9)$$

Equation (8) can be interpreted as follows: Similar to the classical picture in each output 2 or 3, exactly half of the photons  $\frac{|\alpha|^2}{2}$  are reflected or transmitted by means of the balanced BS. The phase shift  $i = e^{i\pi/2}$  of the reflected wave appears automatically. There is no entanglement with respect to coherent states. The result is a product state, as can be seen in (8).

Three important remarks:

a) For  $\alpha = 0$  the coherent state  $|\alpha\rangle$  achieves the vacuum state  $|0\rangle$ , but, e.g., for  $\alpha = 1$  the 1-photon-state  $|1\rangle$  is **not** obtained:  $|\alpha = 1\rangle \neq |1\rangle$ .  $|\alpha = 1\rangle$  and  $|1\rangle$  are entirely different states.

b)  $\frac{1}{\sqrt{2}}(|1\rangle_2|0\rangle_3 + |0\rangle_2|1\rangle_3)$  from (4) can be obtained in no way from  $\left|\frac{i\alpha}{\sqrt{2}}\right\rangle_2 \left|\frac{\alpha}{\sqrt{2}}\right\rangle_3$  of (8) because the first expression is an entangled state (no coincidences are possible) and the last one is a product state. The attempt to call a weak classical field a quantum field is misleading and absolutely incorrect. However, for  $|\alpha|^2 \ll 1$  ( $\alpha \approx \frac{1}{10}$  i.e., weak coherent state) the coherent state can be used very well for generating quantum numbers [25] by considering (8) and (7):

$$\begin{aligned}\left|\frac{i\alpha}{\sqrt{2}}\right\rangle_2 \left|\frac{\alpha}{\sqrt{2}}\right\rangle_3 &\approx |0\rangle_2|0\rangle_3 + \\ &+ \frac{\alpha}{\sqrt{2}} [ |1\rangle_2|0\rangle_3 + |0\rangle_2|1\rangle_3 ] + \dots\end{aligned}\quad (10)$$

As a result, it can be seen that mostly vacuum states are arising, but (with probability  $\frac{|\alpha|^2}{2}$ ) the same entangled state as in (4) appears. Because parametric down-conversion (cf., (4) from Example 1) is a very rare event, the method presented here could be superior.

c) The mean particle number in output mode 2 is

$$\bar{n}_2 = Tr_2(\hat{n}_2\hat{\rho}_2) = \langle 2|_3 \langle \frac{i\alpha}{\sqrt{2}} | \hat{a}_2^\dagger \hat{a}_2 | \frac{i\alpha}{\sqrt{2}} \rangle_2 = \frac{1}{2}|\alpha|^2.\quad (11)$$

The same is valid for output 3.

3) *Input  $|1\rangle_0|1\rangle_1$* : Experimentally, such an input can be possible if the 2 photons simultaneously produced by means of parametric down-conversion are injected in the two input modes.

Photon  $|1\rangle_0$  has two possibilities: either being transmitted or being reflected. The same applies for photon  $|1\rangle_1$ . One

obtains:

$$\begin{aligned}
 |1\rangle_0|1\rangle_1 &= \hat{a}_0^+\hat{a}_1^+|0\rangle_0|0\rangle_1 \xrightarrow{BS} \rightarrow \\
 &\rightarrow \frac{1}{2}(\hat{a}_2^+ + i\hat{a}_3^+)(i\hat{a}_2^+ + \hat{a}_3^+)|0\rangle_2|0\rangle_3 = \\
 &= \frac{i}{2}(\hat{a}_2^+\hat{a}_2^+ + \hat{a}_3^+\hat{a}_3^+)|0\rangle_2|0\rangle_3 = \\
 &= \frac{i}{\sqrt{2}}(|2\rangle_2|0\rangle_3 + |0\rangle_2|2\rangle_3) \quad (12)
 \end{aligned}$$

This equation means entanglement of two photons with vacuum. There are either 2 photons in output 2 or 2 photons in output 3. There are neither coincidences using a balanced BS. But, contrary to a single photon process discussed in example 1, here the appearance of no coincidences is a matter of an interference effect between 2 possibilities of reflection or transmission at the BS.

Thus, we have no coincidences. This is indicated by (12) as well. This fact is experimentally tested in the so-called Hong-Ou-Mandel experiment [26]. A quantum random number generator based on this effect is described in [27].

Completely analog, the density operators  $\hat{\rho}_{23}$ ,  $\hat{\rho}_2$  and  $\hat{\rho}_3$  can be composed using (12). For example, one gets

$$\begin{aligned}
 \hat{\rho}_2 &= \frac{1}{2}(|0\rangle_2\langle 0| + |2\rangle_2\langle 2|) , \\
 \hat{\rho}_3 &= \frac{1}{2}(|0\rangle_3\langle 0| + |2\rangle_3\langle 2|) \\
 \bar{n}_2 &= Tr(\hat{n}_2\hat{\rho}_2) = 1 , \quad \bar{n}_3 = Tr(\hat{n}_3\hat{\rho}_3) = 1 \quad (13)
 \end{aligned}$$

This shows that the two single input photons can be used in order to generate quantum random numbers. This is an additional possibility besides the first case where only one single photon impinges the BS.

4) *Input*  $|\alpha\rangle_0|\beta\rangle_1$ : We discuss a case where two different coherent states  $|\alpha\rangle$  and  $|\beta\rangle$  are taken as input states [28]:

$$\begin{aligned}
 |\alpha\rangle_0|\beta\rangle_1 &= \hat{D}_1(\alpha)\hat{D}_0(\beta)|00\rangle_{01} \xrightarrow{BS} \rightarrow |\gamma\rangle_2|\delta\rangle_3 = \\
 &= |\psi\rangle_{out} \\
 \gamma &= \frac{1}{\sqrt{2}}(\alpha + i\beta) , \quad \delta = \frac{1}{\sqrt{2}}(i\alpha + \beta) . \quad (14)
 \end{aligned}$$

The density operators and mean photon numbers are, therefore,

$$\begin{aligned}
 \hat{\rho}_{23} &= |\psi\rangle_{out}\langle\psi| = |\gamma\rangle_2\langle\gamma| \otimes |\delta\rangle_3\langle\delta| = \hat{\rho}_2 \otimes \hat{\rho}_3 , \\
 \bar{n}_2 &= Tr(\hat{\rho}_2\hat{n}_2) = |\gamma|^2 = \frac{1}{2}(|\alpha|^2 + |\beta|^2) = \\
 &= \bar{n}_3 = |\delta|^2 . \quad (15)
 \end{aligned}$$

Again, for random numbers at the output, we have to require weak coherent input states:

$$\begin{aligned}
 &|\alpha|^2, |\beta|^2 \ll 1 , \rightarrow \\
 &\rightarrow |\psi\rangle_{out} \approx |00\rangle_{23} + (\gamma|10\rangle_{23} + \delta|01\rangle_{23}) . \quad (16)
 \end{aligned}$$

5) *Input*  $|0\rangle_0\frac{1}{\sqrt{2}}(|0\rangle_1+|1\rangle_1)$ : Here, and in the next section, a superposition state  $\frac{1}{\sqrt{2}}(|0\rangle+|1\rangle)$  is combined with a vacuum state  $|0\rangle$  and a one-photon state  $|1\rangle$ , respectively. First, we consider the combination of vacuum with superposition state. The output clearly produces random numbers:

$$\begin{aligned}
 |0\rangle_0\frac{1}{\sqrt{2}}(|0\rangle_1+|1\rangle_1) &= \frac{1}{\sqrt{2}}(1+\hat{a}_1^+)|00\rangle_{01} \xrightarrow{BS} \rightarrow \\
 &\rightarrow \frac{1}{\sqrt{2}}[|00\rangle_{23} + \frac{1}{\sqrt{2}}(i|10\rangle+|01\rangle)_{23}] \quad (17)
 \end{aligned}$$

The mean photon numbers at the output are 1/4 each:

$$\begin{aligned}
 \hat{\rho}_2 &= \frac{1}{2}[|0\rangle_2\langle 0| - \frac{i}{\sqrt{2}}|0\rangle_2\langle 1| + \frac{i}{\sqrt{2}}|1\rangle_2\langle 0| + \\
 &+ \frac{1}{2}|1\rangle_2\langle 1| + \frac{1}{2}|0\rangle_2\langle 0|] \rightarrow \bar{n}_2 = \bar{n}_3 = \frac{1}{4} \quad (18)
 \end{aligned}$$

6) *Input*  $\frac{1}{\sqrt{2}}(|0\rangle_0+|1\rangle_0)|1\rangle_1$ : The combination of superposition with  $|1\rangle$  gives

$$\begin{aligned}
 &\frac{1}{\sqrt{2}}(|0\rangle_0+|1\rangle_0)|1\rangle_1 = \\
 &= \frac{1}{\sqrt{2}}(1+\hat{a}_0^+)\hat{a}_1^+|00\rangle_{01} \xrightarrow{BS} \rightarrow \\
 &\rightarrow \frac{1}{\sqrt{2}}[\frac{1}{\sqrt{2}}(i|10\rangle+|01\rangle)_{23} + \frac{i}{\sqrt{2}}(|20\rangle+|02\rangle)_{23}] = \\
 &= |\psi\rangle . \quad (19)
 \end{aligned}$$

The output state is a mixture of an output state resulting from single photon input and an output state resulting from the Hong-Ou-Mandel-effect. The mean photon number is, therefore, 3/4:

$$\begin{aligned}
 \hat{\rho}_{23} &= |\psi\rangle\langle\psi| \\
 \hat{\rho}_2 &= Tr_3(\hat{\rho}_{23}) = \\
 &= \frac{1}{4}[|1\rangle_2\langle 1| + |1\rangle_2\langle 2| + |0\rangle_2\langle 0| + \\
 &+ |2\rangle_2\langle 1| + |2\rangle_2\langle 2| + |0\rangle_2\langle 0|] \rightarrow \\
 &\rightarrow \bar{n}_2 = \bar{n}_3 = \frac{3}{4} \quad (20)
 \end{aligned}$$

7) *Input*  $|1\rangle_0|\alpha\rangle_1$ : This input is described and discussed in the literature relating to the Mach-Zehnder interferometer using the Wigner function [29][30]. Here, we only consider the action of a BS with intent to create random numbers.

Immediately, we realize that the total number of input photons is  $(1+|\alpha|^2)$ , of course. At the output ports 2 and 3 we expect therefore  $\frac{1}{2}(1+|\alpha|^2)$  each. This is proved below.

Initially, the output state  $|\psi\rangle_{out}$  is calculated as follows:

$$\begin{aligned}
 |1\rangle_0|\alpha\rangle_1 &= \hat{a}_0^+\hat{D}_1(\alpha)|00\rangle_{01} \xrightarrow{BS} \rightarrow \\
 &\rightarrow \frac{1}{\sqrt{2}}(\hat{a}_2^+ + i\hat{a}_3^+)\frac{i\alpha}{\sqrt{2}}|2\rangle_2|\frac{\alpha}{\sqrt{2}}\rangle_3 = |\psi\rangle_{out} . \quad (21)
 \end{aligned}$$

Only for a weak coherent state  $|\alpha\rangle$  random numbers are possible:

$$\begin{aligned}
 |\alpha|^2 \ll 1 \rightarrow |\psi\rangle_{23} &\approx \frac{1}{\sqrt{2}}[|10\rangle + i|01\rangle]_{23} + \\
 &+ \frac{i\alpha}{\sqrt{2}}[|20\rangle + i|02\rangle]_{23} \quad (22)
 \end{aligned}$$

Now, an exact calculation of mean photon number  $\bar{n}_2$  is executed using  $|\psi\rangle_{out}$ . Again, the density operators  $\hat{\rho}_{23}$  and  $\hat{\rho}_2$  are necessary in order to determine  $\bar{n}_2$  using the particle number operator  $\hat{n}_2$ :

$$\hat{\rho}_{23} = |\psi\rangle_{out}\langle\psi| , \quad \hat{\rho}_2 = Tr_3(\hat{\rho}_{23}) , \quad \bar{n}_2 = Tr_2(\hat{\rho}_2\hat{n}_2) \quad (23)$$

The trace-operation is executed by using the completeness relation of Fock states:  $\mathbb{1} = \sum_{n=0}^{\infty} |n\rangle\langle n|$ . We obtain

$$|\psi\rangle_{out} = \frac{1}{\sqrt{2}}[\hat{a}_2^+|\frac{i\alpha}{\sqrt{2}}\rangle_2|\frac{\alpha}{\sqrt{2}}\rangle_3 + i|\frac{i\alpha}{\sqrt{2}}\rangle_2\hat{a}_3^+|\frac{\alpha}{\sqrt{2}}\rangle_3] \quad (24)$$

$$\begin{aligned} \hat{\rho}_2 &= \frac{1}{2} \{ \hat{a}_2^+ | \frac{i\alpha}{\sqrt{2}} \rangle_2 \langle \frac{i\alpha}{\sqrt{2}} | \hat{a}_2 + | \frac{i\alpha}{\sqrt{2}} \rangle_2 \langle \frac{i\alpha}{\sqrt{2}} | (1 + \frac{|\alpha|^2}{2}) - \\ &- i \hat{a}_2^+ | \frac{i\alpha}{\sqrt{2}} \rangle_2 \langle \frac{i\alpha}{\sqrt{2}} | \frac{\alpha}{\sqrt{2}} + i \frac{\alpha^*}{\sqrt{2}} | \frac{i\alpha}{\sqrt{2}} \rangle_2 \langle \frac{i\alpha}{\sqrt{2}} | \hat{a}_2 \} \quad (25) \end{aligned}$$

It can be shown that  $Tr_2(\hat{\rho}_2) = 1$ . For the mean particle number  $\bar{n}_2$  in output 2, we get

$$\begin{aligned} \bar{n}_2 &= \frac{1}{2} \{ 2 \langle \frac{i\alpha}{\sqrt{2}} | \hat{a}_2 \hat{n}_2 \hat{a}_2^+ | \frac{i\alpha}{\sqrt{2}} \rangle_2 + (1 + \frac{|\alpha|^2}{2}) | \frac{i\alpha}{\sqrt{2}} |^2 - \\ &- i 2 \langle \frac{i\alpha}{\sqrt{2}} | \hat{n}_2 \hat{a}_2^+ | \frac{i\alpha}{\sqrt{2}} \rangle_2 \frac{\alpha}{\sqrt{2}} + \\ &+ i \frac{\alpha^*}{\sqrt{2}} 2 \langle \frac{i\alpha}{\sqrt{2}} | \hat{a}_2 \hat{n}_2 | \frac{i\alpha}{\sqrt{2}} \rangle_2 \} = \\ &= \frac{1}{2} (1 + |\alpha|^2) . \quad (26) \end{aligned}$$

In the last step, the property of the trace  $Tr(\hat{A}\hat{B}\hat{C}) = Tr(\hat{B}\hat{C}\hat{A}) = \dots$  has been used. Moreover, one has to consider explicitly that  $\hat{n} = \hat{a}^+ \hat{a}$ . The result in (26) is exactly what we expected. This outcome is valid for arbitrary parameters  $\alpha$ .

8) *Input*  $|\psi\rangle_{in} = \frac{1}{N} (|\alpha\rangle_0 |\beta\rangle_1 + |\beta\rangle_0 |\alpha\rangle_1)$ : This input is a so-called Entangled Coherent State (ECS). It is described and discussed in [28][31][32].

From normalization  ${}_in\langle\psi|\psi\rangle_{in} = 1$  we obtain  $N = \sqrt{2(1 + e^{-|\alpha-\beta|^2})}$  taking account of  $\langle\beta|\alpha\rangle = e^{-|\alpha|^2/2 - |\beta|^2/2 + \alpha\beta^*}$ . In case of  $\alpha = \beta \rightarrow N = 2$ .

The input state can be written as

$$|\psi\rangle_{in} = \frac{1}{N} [\hat{D}_0(\alpha) \hat{D}_1(\beta) + \hat{D}_0(\beta) \hat{D}_1(\alpha)] |00\rangle_{01} . \quad (27)$$

Initially, we discuss the mean photon number of the input. The necessary density operators are

$$\begin{aligned} \hat{\rho}_{01} &= |\psi\rangle_{in} \langle\psi| , \hat{\rho}_0 = Tr_1(\hat{\rho}_{01}) \rightarrow \\ \hat{\rho}_0 &= \frac{1}{N^2} \{ |\alpha\rangle_0 \langle\alpha| + |\beta\rangle_0 \langle\beta| + e^{-|\alpha|^2/2 - |\beta|^2/2} \times \\ &\times [ |\beta\rangle_0 \langle\alpha| e^{\alpha\beta^*} + |\alpha\rangle_0 \langle\beta| e^{\alpha^*\beta} ] \} . \quad (28) \end{aligned}$$

Here  $\sum_n | \langle n|\alpha\rangle |^2 = 1$  and  $\langle n|\alpha\rangle = \frac{\alpha^n}{\sqrt{n!}} e^{-|\alpha|^2/2}$  have been used. It can easily be shown that  $Tr(\hat{\rho}_0) = 1$ .

The mean number of input-photons  $\bar{n}_0$  is obtained after some manipulation :

$$\begin{aligned} \bar{n}_0 &= Tr(\hat{\rho}_0 \hat{n}) = \\ &= \frac{1}{N^2} \{ |\alpha|^2 + |\beta|^2 + e^{-|\alpha|^2 - |\beta|^2 + \alpha\beta^* + \alpha^*\beta} \times \\ &\times [ \alpha\beta^* + \alpha^*\beta ] \} . \quad (29) \end{aligned}$$

An equivalent expression is obtained for  $\bar{n}_1$ . For  $\alpha = \beta \rightarrow \bar{n}_0 = |\alpha|^2$ ,  $|\psi\rangle_{in} = |\alpha\alpha\rangle_{01}$ .

Now, the output is considered. From (27) one gets directly (using the BS-process  $\rightarrow^{BS}\rightarrow$ ) the normalized output state

$$\begin{aligned} |\psi\rangle_{out} &= \frac{1}{N} [ | \frac{\alpha + i\beta}{\sqrt{2}} \rangle_2 | \frac{i\alpha + \beta}{\sqrt{2}} \rangle_3 + \\ &+ | \frac{i\alpha + \beta}{\sqrt{2}} \rangle_2 | \frac{\alpha + i\beta}{\sqrt{2}} \rangle_3 ] , \quad (30) \end{aligned}$$

taking into account the Baker-Champbell-Hausdorff-theorem.

**Special case :**  $\beta = -i\alpha$

$$\begin{aligned} |\psi\rangle_{out} &= \frac{1}{N} [ | \sqrt{2}\alpha \rangle_2 | 0 \rangle_3 + | 0 \rangle_2 | \sqrt{2}\alpha \rangle_3 ] , \\ N &= \sqrt{2(1 + e^{-2|\alpha|^2})} . \quad (31) \end{aligned}$$

This is a coherent state  $|\sqrt{2}\alpha\rangle$  in equal superposition of being in either one of two possible paths 2 or 3. This expression can be used in order to create random numbers. We calculate mean photon numbers:

$$\begin{aligned} \hat{\rho}_{23} &= |\psi\rangle_{out} \langle\psi| , \hat{\rho}_2 = Tr_3(\hat{\rho}_{23}) \rightarrow \\ \hat{\rho}_2 &= \frac{1}{N^2} \{ | \sqrt{2}\alpha \rangle_2 \langle \sqrt{2}\alpha | + \\ &+ | 0 \rangle_2 \langle 0 | + e^{-|\alpha|^2} [ | 0 \rangle_2 \langle \sqrt{2}\alpha | + | \sqrt{2}\alpha \rangle_2 \langle 0 | ] \} \quad (32) \end{aligned}$$

As before:  $Tr(\hat{\rho}_2) = 1$ .

$$\bar{n}_2 = Tr(\hat{\rho}_2 \hat{n}) = \frac{|\alpha|^2}{1 + e^{-2|\alpha|^2}} (= \bar{n}_3) . \quad (33)$$

(  $|\alpha|^2 \ll 1 \rightarrow \bar{n}_2 \approx |\alpha|^2/2$ ,  $|\alpha|^2 \gg 1 \rightarrow \bar{n}_2 \approx |\alpha|^2$  . ) Putting  $\beta$  to be  $-i\alpha$  already at the input, one obtains  $\bar{n}_0 = \bar{n}_2$  of course (see (29)).

9) *Input*  $|\psi\rangle_{01} = |\beta\rangle_0 \frac{1}{N_\beta} (|\beta\rangle_1 + |-\beta\rangle_1)$ : This input means that we have a mixture of a coherent state  $|\beta\rangle_0$  in mode 0 with a CSS (Coherent Superposition State [28][32]–[34]) in mode 1. The normalization of the wave function yields

$${}_01\langle\psi|\psi\rangle_{01} = 1 \rightarrow N_\beta = \sqrt{2(1 + e^{-2|\beta|^2})} . \quad (34)$$

Now, we apply a BS which operates with the well-known Hadamard-transformation  $\hat{H}$ :

$$\begin{pmatrix} \hat{a}_2 \\ \hat{a}_3 \end{pmatrix} = \frac{1}{\sqrt{2}} \begin{pmatrix} 1 & 1 \\ 1 & -1 \end{pmatrix} \begin{pmatrix} \hat{a}_0 \\ \hat{a}_1 \end{pmatrix} = \hat{H} \begin{pmatrix} \hat{a}_0 \\ \hat{a}_1 \end{pmatrix} . \quad (35)$$

This transformation means transmission from the back side with phase  $-1 = e^{i\pi}$ , that is to say (see Figure 1):

$$\hat{a}_0^+ = \frac{1}{\sqrt{2}} (\hat{a}_2^+ + \hat{a}_3^+) , \hat{a}_1^+ = \frac{1}{\sqrt{2}} (\hat{a}_2^+ - \hat{a}_3^+) . \quad (36)$$

The input state is easily transformed and the output becomes a coherent state  $|\sqrt{2}\beta\rangle$  entangled with the vacuum  $|0\rangle$ :

$$|\psi\rangle_{01} = \hat{D}_0(\beta) \frac{1}{N_\beta} [ \hat{D}_1(\beta) + \hat{D}_1(-\beta) ] |00\rangle_{01} , \quad (37)$$

$\rightarrow^{BS(\hat{H})} \rightarrow$

$$|\psi\rangle_{23} = \dots = \frac{1}{N_\beta} [ | \sqrt{2}\beta \rangle_2 | 0 \rangle_3 + | 0 \rangle_2 | \sqrt{2}\beta \rangle_3 ] \quad (38)$$

Differently expressed, we have a coherent state  $|\sqrt{2}\beta\rangle$  in equal superposition of being in either one of two possible paths 2 or 3. This is the same result we have obtained in (31) denoting  $\beta$  by  $\alpha$ , however a Hadamard transformation is used for the BS.

### III. CONCLUSION

In this paper, we provide insights into the complexity of generating true random numbers with Beam Splitters for cryptographic devices. Moreover, we investigate pre-defined input configurations and adopt mathematical procedures for a 50:50 Beam Splitter to derive true random data sets inside of a Hardware Security Module. The variants of the inputs are proposed, each of which are obtaining varying outputs.

As a result, we show the capability to use 50:50 Beam Splitters as quantum random number generators. We believe that the demonstrated input configurations of the quantum random number generator provide a suitable alternative to deterministic random number generators and increase the security of cryptographic devices and particularly of HSMs.

### REFERENCES

- [1] D. Fox, "Hardware Security Module (HSM)," *Datenschutz und Datensicherheit - DuD*, vol. 33, no. 9, pp. 564–564, Sep. 2009.
- [2] B. Hamid and D. Weber, "Engineering secure systems: Models, patterns and empirical validation," *Computers & Security*, vol. 77, pp. 315 – 348, 2018.
- [3] R. De Prisco, A. De Santis, and M. Manna, "Reducing Costs in HSM-Based Data Centers," in *International Conference on Green, Pervasive, and Cloud Computing*, ser. Theoretical Computer Science and General Issues, M. H. A. Au, A. Castiglione, K.-K. R. Choo, F. Palmieri, and K.-C. Li, Eds. Springer International Publishing AG, 2017, pp. 3–14.
- [4] J. A. Buchmann, E. Karatsiolis, and A. Wiesmaier, *Introduction to Public Key Infrastructures*. Springer Publishing Company, Incorporated, 2013.
- [5] T. Zefferer, "A server-based signature solution for mobile devices," in *The 12th International Conference on Advances in Mobile Computing and Multimedia*, Dec. 2014, pp. 175–184.
- [6] E. Shmueli, R. Vaisenberg, E. Gudes, and Y. Elovici, "Implementing a database encryption solution, design and implementation issues," *Computers & Security*, vol. 44, pp. 33–50, Jul. 2014.
- [7] *Federal Information Processing Standards Publication 140-2 (FIPS PUB 140-2)*, National Institute of Standards and Technology Std., May 2001.
- [8] *Federal Information Processing Standards Publication 140-3 (FIPS PUB 140-3), Security Requirements for Cryptographic Modules*, National Institute of Standards and Technology Std., Mar. 2019.
- [9] *Common Criteria for Information Technology Security Evaluation Part 1: Introduction and general model, Version 3.1, Revision 5, CCMB-2017-04-001*, The Common Criteria Working Group Std., Apr. 2017.
- [10] *Common Criteria for Information Technology Security Evaluation Part 2: Security functional components, Version 3.1, Revision 5, CCMB-2017-04-002*, The Common Criteria Working Group Std., Apr. 2017.
- [11] *Common Criteria for Information Technology Security Evaluation Part 3: Security assurance components, Version 3.1, Revision 5, CCMB-2017-04-003*, The Common Criteria Working Group Std., Apr. 2017.
- [12] *ISO/IEC 15408-1:2009, Information technology Security techniques Evaluation criteria for IT security Part 1: Introduction and general model*, International Organization for Standardization/International Electrotechnical Commission (ISO/IEC) Std., Jan. 2014.
- [13] *ISO/IEC 15408-2:2008, Information technology Security techniques Evaluation criteria for IT security Part 2: Security functional components*, International Organization for Standardization/International Electrotechnical Commission (ISO/IEC) Std., Jun. 2011.
- [14] *ISO/IEC 15408-3:2008, Information technology Security techniques Evaluation criteria for IT security Part 3: Security assurance components*, International Organization for Standardization/International Electrotechnical Commission (ISO/IEC) Std., Jun. 2011.
- [15] E. Barker and J. Kelsey, *Recommendations for random number generation using deterministic random bit generators (NIST Special Publication 800-90A Revision 1)*, National Institute of Standards and Technology Std., Jun. 2015.
- [16] A. Stefanov, N. Gisin, O. Guinnard, L. Guinnard, and H. Zbinden, "Optical quantum random number generator," *Journal of Modern Optics*, vol. 47, no. 12, pp. 595–598, Mar. 2000.
- [17] T. Jennewein, U. Achleitner, G. Weihs, H. Weinfurter, and A. Zeilinger, "A fast and compact quantum random number generator," *Review of Scientific Instruments*, vol. 71, no. 4, Apr. 2000.
- [18] D. Marangon, A. Plews, M. Lucamarini, J. Dynes, A. Sharpe, Z. Yuan, and A. Shields, "Long term test of a fast and compact quantum random number generator," *Journal of Lightwave Technology*, vol. 36, no. 17, pp. 3778–3784, May 2018.
- [19] K. Svozil, "Three criteria for quantum random-number generators based on beam splitters," *Physical Review A*, vol. 79, p. 054306, May 2009.
- [20] L. Mandel and E. Wolf, *Optical Coherence and Quantum Optics*. Cambridge: Cambridge University Press, 1995.
- [21] U. Leonhardt, P. Knight, and A. Miller, *Measuring the Quantum State of Light*, ser. Cambridge Studies in Modern Optics. Cambridge: Cambridge University Press, 1997.
- [22] R. Loudon, *The Quantum Theory of Light*. Oxford: OUP Oxford, 2000.
- [23] W. P. Schleich, *Quantum Optics in Phase Space*. Berlin: Wiley-VCH Verlag Berlin GmbH, Feb. 2005.
- [24] C. Gerry and P. L. Knight, *Introductory Quantum Optics*. Cambridge: Cambridge University Press, 2005.
- [25] J. G. Rarity, P. Owens, and P. R. Tapster, "Quantum random-number generation and key sharing," *Journal of Modern Optics*, vol. 41, no. 12, pp. 2435–2444, Jan. 1994.
- [26] C. K. Hong, Z. Y. Ou, and L. Mandel, "Measurement of subpicosecond time intervals between two photons by interference," *Physical Review Letters*, vol. 59, no. 18, pp. 2044–2046, Nov. 1987.
- [27] O. Kwon, Y.-W. Cho, and Y.-H. Kim, "Quantum random number generator using photon-number path entanglement," *Applied Optics*, vol. 48, no. 9, pp. 1774–1778, Mar. 2009.
- [28] B. C. Sanders, "Entangled coherent states," *Physical Review A*, vol. 45, pp. 6811–6815, May 1992.
- [29] X. Xu, F. Jia, L. Hu, Z. Duan, Q. Guo, and S.-j. Ma, "Quantum interference between an arbitrary-photon Fock state and a coherent state," *Journal of Modern Optics*, vol. 59, no. 18, pp. 1624–1633, Oct. 2012.
- [30] A. Windhager, M. Suda, C. Pacher, M. Peev, and A. Poppe, "Quantum interference between a single-photon Fock state and a coherent state," *Optics Communications*, vol. 284, no. 7, pp. 1907–1912, Apr. 2011.
- [31] B. C. Sanders, "Review of entangled coherent states," *Journal of Physics A Mathematical and Theoretical*, vol. 45, no. 24, p. 244002, Dec. 2011.
- [32] Y. Israel, L. Cohen, X.-B. Song, J. Joo, H. S. Eisenberg, and Y. Silberberg, "Entangled coherent states created by mixing squeezed vacuum and coherent light," 2019. [Online]. Available: <https://arxiv.org/abs/1707.01809>
- [33] C. Gerry and P. L. Knight, "Quantum superpositions and Schrödinger cat states in quantum optics," *American Journal of Physics*, vol. 65, no. 10, pp. 964–974, Oct. 1997.
- [34] H. Jeong and M. S. Kim, "Efficient quantum computation using coherent states," *Physical Review A*, vol. 65, p. 042305, Mar. 2002.

## Analysis, Design and Performance Evaluation of On-Chip Optical Wireless Links

Jinous Shafiei Dehkordi  
Velio Tralli

Engineering Department  
University of Ferrara  
Ferrara, Italy  
Email: shfjns@unife.it  
velio.tralli@unife.it

Marina Barbiroli  
Jacopo Nanni  
Franco Fuschini

DEI - University of Bologna, Italy  
Email: marina.barbiroli@unibo.it  
jacopo.nanni3@unibo.it  
franco.fuschini@unibo.it

Vincenzo Petruzzelli

Polytechnic of Bari  
Bari, Italy  
Email: vincenzo.petruzzelli@poliba.it

**Abstract**—In Network-on-Chips (NoCs), Optical Wireless (OW) interconnects have recently gained attention to overcome the limitations of existing wired and wireless Radio Frequency (RF) technologies, while preserving the bandwidth and delay characteristics of optical interconnects. In this paper, we investigate the communication performance of the on-chip OW links by considering the effects of both wireless propagation and inter-link interference, which arises when the same optical frequency is used for multiple transmissions in a NoC. A Ray Tracing (RT) approach is applied to the layered structure of the on-chip wireless channel to obtain accurate modeling of multipath propagation. By using the Ray Tracing (RT) results, the Bit Error Probability (BEP) is evaluated as a function of desired and interfering signal powers, which depend on the far-field spatial fading conditions. The physical parameters and the geometry of the scenario, and the impact of antenna radiation pattern are taken into account in the evaluation. The analysis and the results enable system designers to design and provide efficient on-chip interconnects, optimizing not only the topology of the OW links in the NoC, but also the physical parameters of the links, including antenna characteristics, that influence the wireless communication.

**Keywords**—Optical wireless links; On-chip communications; Performance evaluation; Ray tracing.

### I. INTRODUCTION

Optical Wireless (OW) links have recently emerged as an interconnection technology for Network-on-Chips (NoCs) [1] [2]. The NoC technology [3] requires highly reliable communications among multiple processing cores, whereas interconnecting on-chip components is a long-standing problem [4][5]. The continuously growing need for low-power and high-speed communication asks for efficient on-chip interconnects. The number of nodes in NoCs is predicted to increase significantly in the near future. In such networks, the traditional scaling of metal interconnections cannot satisfy the communication requirements due to their limitations in power consumption and bandwidth. To overcome these problems, alternative approaches like optical interconnections using silicon photonics [6][7] and wireless interconnections using Radio Frequency (RF) technologies [8]–[11], were considered.

Optical NoCs exploit optical frequency to provide high data rate communication, while reducing propagation losses

and delays [6][7]. However, as the number of on-chip cores increases, the realization of optical NoCs with wired architecture becomes very complicated, which is followed by increasing complexity of switching and routing, and power losses due to multiple waveguide crossings. Providing point-to-point communication between cores and the limitations of wired architectures to support multi-cast and broadcast transmissions are the main challenges of such networks.

Wireless communication has gained a wide interest for multicore system-on-chip as an efficient solution to replace long distance on-chip interconnects [9][10], thus simplifying routing and layout complexity. Wireless on-chip communications also reduce latency and power consumption, and improve broadcast communications in large-scale chip multi-processors [12]. However, RF wireless communications cannot provide the same bandwidth as optical technology, and present significant challenges for on-chip antenna integration [13].

OW interconnects can take advantages of both the optical and wireless communication [1][2]. This on-chip interconnect technology exploits broadcast and multicast transmissions at optical frequencies with simple network architectures and efficient use of the chip area. The OW links can be realized by coupling optical nanoantennas with optical waveguides, where the same wavelength propagating on optical waveguides can be used for wireless connections. Therefore, there is no need for any electro-optical conversion and increasing power consumption, and latency. Nevertheless, there are several challenges for using OW links in NoCs that must be addressed accurately. The OW links operating on the same wireless channel (optical wavelength) may interfere with each other, which degrades communication performance [14].

We aim to study the effects of both wireless propagation and interference on the communication performance in NoCs using OW links. The antenna radiation pattern, the geometry of the scenario and the various parameters characterizing the layered structure of the chip are considered. In particular, propagation channel is characterized by using a RT method, which tracks multipath fading in the on-chip wireless channel [15]. The Bit Error Probability (BEP) is evaluated as a function of desired

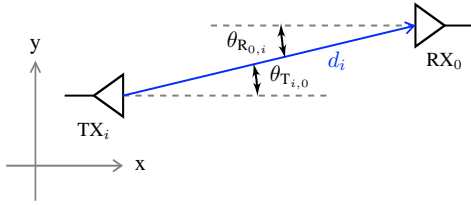


Figure 1. Top view of a OW link.

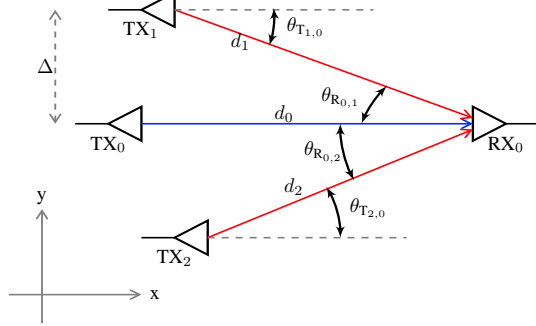


Figure 2. Top view of multiple OW links.

and interfering signal powers, which are subject to far-field spatial fading. The results allow a system designer to find the optimal OW links configuration in the NoC, such that a specified BEP is satisfied for the on-chip communications.

The remainder of this paper is organized as follows. Section II presents the scenario of the NoC. In Section III, the propagation channel is modeled in the layered structure of the chip. Section IV describes the system model and evaluates the BEP considering both interference and noise in the NoC. Section V provides some numerical results for different network configurations. Finally, Section VI gives our conclusions.

## II. ON-CHIP COMMUNICATION SCENARIO

Consider a NoC, where nodes are communicating through OW links. For each link, the source of the optical power is an external off-chip laser coupled to an optical bus or waveguide. Then, a Micro Ring Resonator (MRR) carries out both electrical-to-optical conversion and digital modulation of the optical carrier. Finally, the modulated signal is radiated within the chip through the optical antenna. At the receiving end of the wireless link, the optical impinging signal is seized by the optical receiving antenna, filtered by a second MRR and converted by a photodiode into the electrical domain.

The frequency reuse concept is used to improve spectrum efficiency. By reusing the same optical wavelength in multiple links, the number of simultaneous communications will not be limited by the number of available wavelengths. In particular, we consider the general case where there are  $N + 1$  wireless links that use the same frequency and may interfere with each other. Figure 1 shows the top view of the wireless part of a single link, where the antenna of the probe receiver

$RX_0$  receives the optical signal from the antenna of the  $i$ -th transmitter  $TX_i$ . The distance between the antennas is  $d_i$ . In the figure, dashed lines show the antenna axes,  $\theta_{T_{i,0}}$  is the angle between the transmitting direction and  $TX_i$  antenna axis, and  $\theta_{R_{0,i}}$  is the angle between the receiving direction and  $RX_0$  antenna axis. Figure 2 shows a scenario with multiple links, where the desired link is interfered by the adjacent links, i.e.,  $TX_1$  and  $TX_2$ . We use index  $i = 0$  ( $TX_0$ ) for the transmitting side of the desired link, and indexes  $i = 1, 2, \dots, N$  for the interfering links. We assume that the transmit antenna of  $TX_0$  is located at the position  $(x_{TX_0}, y_{TX_0}) = (0, 0)$  in the horizontal plane. The receive antenna of  $RX_0$  is located at distance  $d_0 = (x_{RX_0}^2 + y_{RX_0}^2)^{1/2}$  from  $TX_0$ , and is rotated versus the  $TX_0$  antenna. Thus, the maximum gain for transmitting and receiving antennas in the desired link is achieved.

As long as a single link is considered, communication errors are mainly due to the propagation conditions and to the noise effect that influence the optical system. In contrast, if a multi-link scenario is addressed, mutual interference can arise between the simultaneous links, to an extent that depends on antenna radiation patterns and reciprocal positions of the interfering links.

## III. CHANNEL MODELING

We use a 3D RT to characterize the far-field spatial fading of the on-chip wireless channel [15]. In particular, we refer to the optical frequency of 193.5 THz, corresponding to wavelength  $\lambda = 1.55 \mu m$  in vacuum. The layered structure of the chip and the electromagnetic properties of the materials are also considered in the analysis. Figure 3 shows the side view (in  $xz$  plane) of each OW link in Figure 1. The transmit and receive antennas are placed at the middle of a homogenous  $SiO_2$  layer with the thickness  $h_{slb}$  in the range of (4-10)  $\mu m$ . The thickness of the up and down layers are denoted by  $h_{up}$  and  $h_{down}$ , respectively. Wave propagation occurs within the  $SiO_2$  slab, which experiences reflections from the interfaces with surrounding mediums, thus causing multipath effects [1] [2][15]–[17]. The upper medium above the  $SiO_2$  layer can be air or a different passivation material, the down layer can be silicon or metal. By considering the chip layered structure, multipath is fundamentally generated by multiple reflections between the interfaces of different media (see Figure 3), which can be evaluated by using the RT approach as in [1][15]. Note that the RT modeling is particularly employed for the investigation of the optical wireless channel, as geometrical optic is expected to become more reliable as frequency increases.

In the RT simulations, both geometrical and electromagnetic properties of the wireless links have to be taken into account. The geometrical parameters include the  $SiO_2$  layer thickness ( $h_{slb}$  in Figure 3), the antenna distance from the interfaces ( $z = 0$  is at the middle of the  $SiO_2$  layer with the same distances from the upper and lower interfaces) and the wireless link length (i.e., distance between transmitting and receiving antennas). The electromagnetic parameters include the material refractive index of each layer of the chip ( $n_{down}$ ,  $n_{slb}$  and

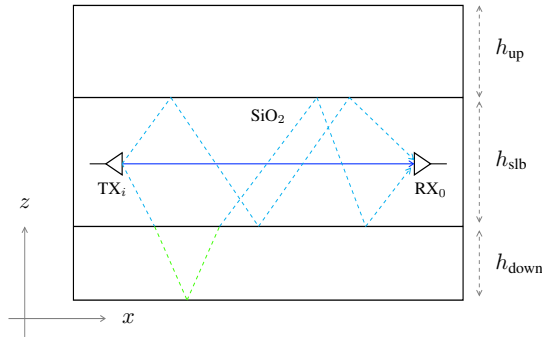


Figure 3. Side view of chip layered structure.

$n_{\text{up}}$ ). A 3D representation of the antenna radiation patterns is also necessary for RT modeling. The assessment carried out in this work is based on an idealized model for the antenna radiation diagram, but any other antenna configurations can be embedded into the RT tool. In particular, the gain of the antenna in a given direction is determined by the following expression.

$$g(\alpha, \phi) = \begin{cases} 10 \log_{10}(G \cos(\phi)^n \cos(\pi/2 - \alpha)^n) & \text{if } |\phi| < \frac{\pi}{2} \\ -50 \text{ dB} & \text{otherwise} \end{cases} \quad (1)$$

where  $n = (10^{0.1 G_{\text{dB}}})/2 - 1$ ,  $G$  is the antenna gain,  $\alpha$  is the elevation angle and  $\phi$  the azimuth angle. Although rays in Figure 3 lie in the vertical ( $xz$ ) plane, the 3D representation of the antenna radiation pattern is necessary, in order for the RT simulation to be run irrespective of the antenna orientation with respect to the propagation plane, e.g., to estimate the power arriving from an interfering transmitter. Once the rays have been tracked and the fields impinging on the receiver have been computed, the overall received power can be evaluated as illustrated in [15]. The important parameters considered for the RT simulations are summarized in Table I.

#### IV. SYSTEM MODELING AND PERFORMANCE EVALUATION

The performance of a communication link is usually characterized in terms of BEP, or measured as bit error rate from an experimental setting. For the design of networks with wireless links, it is very important to adopt an interference-aware framework for BEP evaluation, exploiting the analysis carried out in [18]. Cross-link interference may occur among simultaneously transmitting links that use the same optical channel, as illustrated in Section II. Within this framework, a network designer can find the optimal link configurations that meet the required performance for on-chip communication. For the performance analysis, we assume that all links use intensity modulation On-Off Keying (OOK) with Non-Return-to-Zero (NRZ) pulses and direct detection. If the bits of the data sources have the same probability  $1/2$ , the average power of the modulated signal is one half of the power of the unmodulated carrier, also named here as optical power. The optical power of the received desired signal is denoted by  $P_0$ , and the optical

TABLE I. RT PARAMETERS.

RT simulation parameters	
$h_{\text{up}}$	$\infty$
$h_{\text{slb}}$	4-10 $\mu\text{m}$
$h_{\text{down}}$	$\infty$
$d_0$	30-1500 $\mu\text{m}$
$f$	193.5 THz
$n_{\text{down}}$	3.47 (Silicon, metal otherwise)
$n_{\text{slb}}$	1.44 (Silica)
$n_{\text{up}}$	1 (Air)
antenna Gain	15-25 dB

power of the  $i$ -th received interfering signal, normalized to the desired optical power, is denoted by  $x_i = P_i/P_0$ , with  $i = 1, 2, \dots, N$ . The received powers are functions of the geometry of the links, the distances and the angles between the antennas, the antenna design, the propagation characteristics of each link. For a given transmitted optical power,  $P_T$ , the received power is given by  $P_i = GP_i P_T$ , where  $GP_i$  is the path gain of the channel between transmitter  $i$  and reference receiver, which is obtained with the RT tools, as shown in Section III.

The BEP is one of the principal metrics that allows to describe the overall communication performance, which is evaluated as the function of Signal-to-Noise Ratio (SNR) and interference powers ( $x_i$ 's). In the analysis,  $\text{SNR} = 4\gamma^2$ ,  $\gamma = \eta_{\text{PD}} P_0 / (2\sigma_{\text{th}})$  depends on the unmodulated received power,  $\eta_{\text{PD}}$  is the responsivity of photodetector, and  $\sigma_{\text{th}}$  is the standard deviation of the additive Gaussian noise at the receiver. The dominant noise at the  $p$ - $i$ - $n$  receivers usually is the thermal noise [19]. Therefore, noise variance  $\sigma_{\text{th}}^2$  does not depend on transmitted bits and is given by  $\sigma_{\text{th}}^2 = 4KT_{\text{eq}}/(2R_L T)$ , where  $K$  is the Boltzman's constant,  $T_{\text{eq}}$  is the noise temperature of the receiver,  $R_L$  is the resistance of the receiver and  $T = 1/R_b$  is the bit interval of data transmission with  $R_b$  the data-rate of the links. Recall that the probability of detecting the photocurrent transmitting *zero* above the decision threshold, or detecting the photocurrent transmitting *one* below the threshold at the receiver is evaluated as the BEP. In particular, the BEP is given by  $\bar{P}_b(\gamma, x_1, \dots, x_I) = \mathbb{E}\{P_{b|b_i, \phi_i, \tau_i}(\gamma, x_1, \dots, x_N)\}$  through the analytical method in [18], where  $\mathbb{E}\{\cdot\}$  is the expected value taken over the Random Variables (RVs) in the optical wireless communication system. The RVs include the transmitted bits  $b_i$  with one-half probability of being one or zero, the phases  $\phi_i$  of the optical carriers at the receiver and the time offsets  $\tau_i$  of the asynchronous interfering links, which are uniformly distributed on  $[0, 2\pi]$  and  $[0, T]$ , respectively, for  $i = 1, \dots, N$ .

#### V. NUMERICAL RESULTS

We examine some link scenarios by using the experimental measurements from RT. The principal parameters are given in Table I. In the results, the chip is assumed to be sufficiently large, such that the reflected rays from the lateral sides in the  $xy$  plane can be neglected. For example, consider a distance of

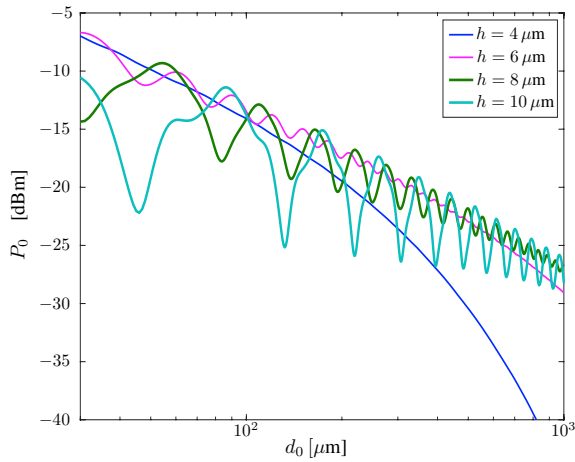


Figure 4. Received power vs distance  $d_0$  with  $G = 20$  dB and different values of  $h_{\text{slb}}$  [ $\mu\text{m}$ ] without interfering link

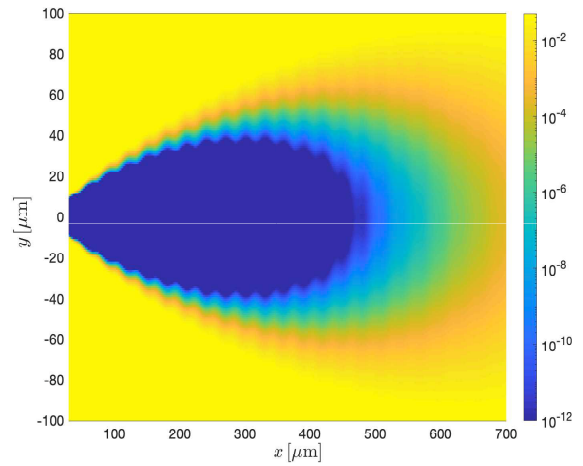


Figure 6. BEP vs position of  $\text{RX}_0$  antenna in the  $xy$  plane with  $G = 20$  dB,  $h_{\text{slb}} = 6 \mu\text{m}$ , and without interfering link.

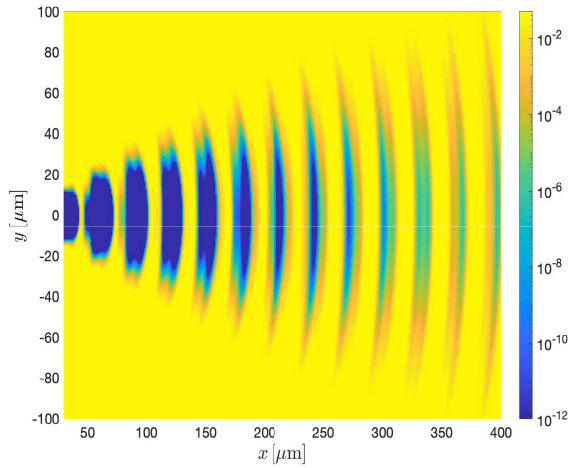


Figure 5. BEP vs position of  $\text{RX}_0$  antenna in the  $xy$  plane with  $G = 15$  dB,  $h_{\text{slb}} = 6 \mu\text{m}$ , and without interfering link.

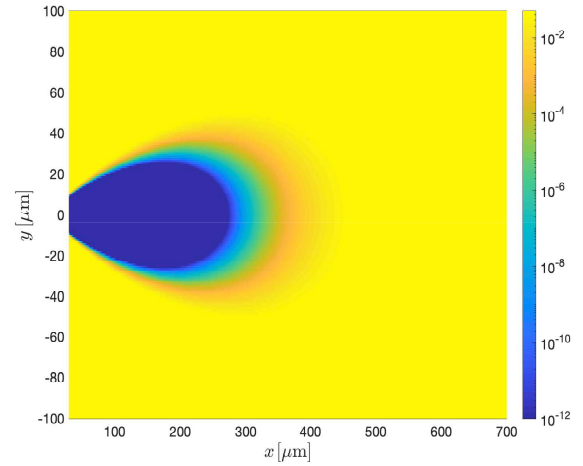


Figure 7. BEP vs position of  $\text{RX}_0$  antenna in the  $xy$  plane with  $G = 20$  dB,  $h_{\text{slb}} = 4 \mu\text{m}$ , and without interfering link.

at least  $500 \mu\text{m}$  from transmit/receive antennas to the lateral sides of the chip. Therefore, only the reflections from the interfaces between the  $\text{SiO}_2$  slab, and upper and lower layers ( $xz$  plane) contribute to the aggregate received signal. The  $\text{TX}_0$  is located at the origin of the 3D coordinate system ( $x_{\text{TX}_0} = y_{\text{TX}_0} = z_{\text{TX}_0} = 0$ ), where  $z = 0$  at the middle of the  $\text{SiO}_2$  slab and for all transmitters and receivers  $z = 0$ . For all results, the average power of all the transmitted signals is 0 dBm, the data-rate is  $R_b = 10$  Gbit/s and the parameters of the receiver are  $\eta_{\text{PD}} = 0.7$  A/W,  $T_{\text{eq}} = 600$  K,  $R_L = 1000 \Omega$ . Figure 4 shows the received power  $P_0$  in dBm vs the distance of  $d_0 \mu\text{m}$  for the wireless link as shown in Figure 1, when the antennas of  $\text{TX}_0$  and  $\text{RX}_0$  are aligned, i.e.,  $\theta_{\text{T}_{0,0}} = \theta_{\text{R}_{0,0}} = 0$ . The results are provided for the antennas with  $G = 20$  dB and different values of the slab layer thickness ( $h_{\text{slb}}$ ). It is shown that by increasing the thickness, the fluctuations of the results increase and at large distances, the power level

decays slowly with higher thickness compared to the cases with smaller thickness.

Figures 5 to 7 map the BEP over the positions of the antenna of receiver  $\text{RX}_0$  in a two dimensional  $xy$  plane, when the antenna of the desired transmitter  $\text{TX}_0$  is located at the origin ( $x = 0, y = 0$ ) and the interfering link is absent. The values of the BEP are shown by colorbars. The antenna gain is  $G = 15$  dB with  $h_{\text{slb}} = 6 \mu\text{m}$  in Figure 5, whereas  $G = 20$  dB, and  $h_{\text{slb}} = 4 \mu\text{m}$  and  $6 \mu\text{m}$  are considered in Figures 7 and 6, respectively. The area with  $P_b \leq 10^{-8}$  can be considered as a *coverage* domain for the given setting (blue domain). As shown, the *coverage* domain in Figure 5 is not regular, which is due to received power fluctuations resulting from multipath propagation. The domain is composed of a number of separated zones and the maximum coverage distance achievable without interruptions is limited to  $40 \mu\text{m}$ . By increasing the antenna gain the *coverage* domain

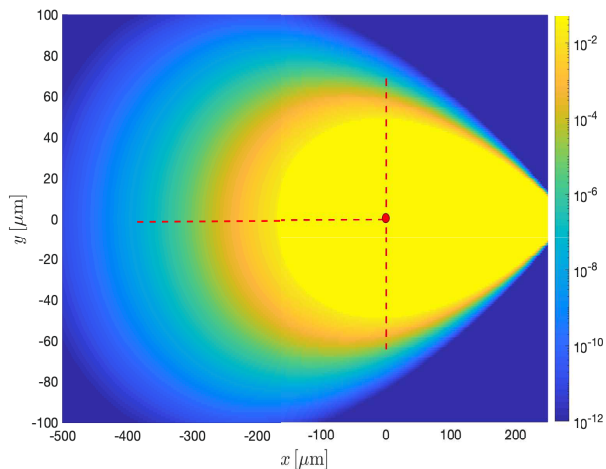


Figure 8. BEP vs position of TX<sub>1</sub> antenna in the  $xy$  plane with  $G = 20$  dB,  $h_{\text{slb}} = 4 \mu\text{m}$ , where  $d_0 = 280 \mu\text{m}$ .

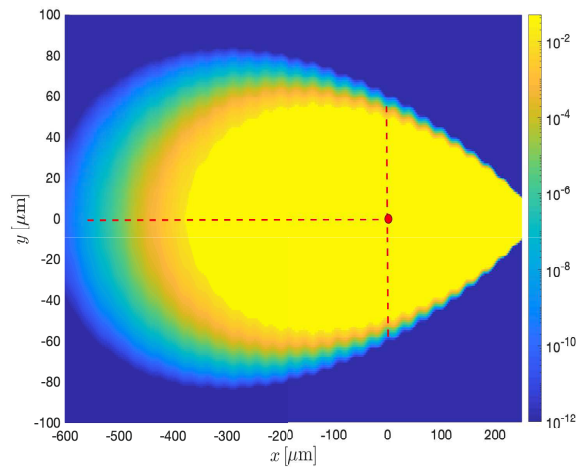


Figure 9. BEP vs position of TX<sub>1</sub> antenna in the  $xy$  plane with  $G = 20$  dB,  $h_{\text{slb}} = 6 \mu\text{m}$ , where  $d_0 = 280 \mu\text{m}$ .

becomes larger and continuous, as shown in Figures 6 and 7. In fact, by reducing the antenna beamwidth, also the multipath induced power fluctuations become small. The coverage is guaranteed for a maximum distance of roughly  $480 \mu\text{m}$  in Figure 6. Received power fluctuations can be further reduced by decreasing the slab thickness, as shown in Fig 7 for  $h_{\text{slb}} = 4 \mu\text{m}$ . However, the coverage distance decreases to roughly  $280 \mu\text{m}$  for  $h_{\text{slb}} = 4 \mu\text{m}$ . This happens because, with few multipath components the received power decreases more rapidly at large distances, as seen in Figure 4.

In Figures 9, 10 and 11, the BEP values are mapped over the positions of an interfering transmitter TX<sub>1</sub> in two dimensional  $xy$  plane, where the antennas of TX<sub>0</sub> and RX<sub>0</sub> are aligned and the distance  $d_0$  is fixed to a given value. Note that  $d_0$  is selected inside the *coverage* domain, as mentioned for example in Figure 7 and Figure 6.

Figure 8 and Figure 9 examine  $h_{\text{slb}} = 4$  and  $6 \mu\text{m}$ , respectively, to provide a comparison between different values of the slab thickness, considering  $G = 20$  dB and  $d_0 = 280 \mu\text{m}$  (inside the *coverage* area for both cases). The red point at the origin ( $x = 0, y = 0$ ) shows the desired transmitter position. Here, we denote the domain with  $P_b \geq 10^{-8}$  (green-yellow domain) as *not allowed* domain for an adjacent transmitter that interfere with the desired link. It can be observed that the case with  $h = 6 \mu\text{m}$  experiences more fluctuations in the BEP values since both the useful and interfering signals are subject to more fading with respect to the case with  $h_{\text{slb}} = 4 \mu\text{m}$ . Consider an interfering link parallel to the desired one, i.e.,  $x = 0, y \neq 0$  for the adjacent transmitter. In order to maintain  $P_b \leq 10^{-8}$ , the adjacent transmitter cannot be placed on the vertical dashed line, thus  $\Delta = |y| \geq 74 \mu\text{m}$ . By increasing  $h_{\text{slb}}$  in Figure 9,  $\Delta$  decreases to  $45 \mu\text{m}$ , therefore, for parallel links increasing the thickness can reduce the reuse distance. Consider an interfering link aligned to the desired one, ( $x \neq 0, y = 0$ ) with a transmitter that has the same

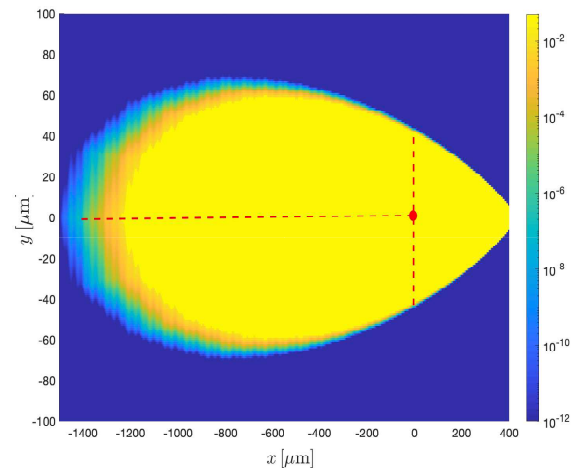


Figure 10. BEP vs position of TX<sub>1</sub> antenna in the  $xy$  plane with  $G = 25$  dB,  $h_{\text{slb}} = 6 \mu\text{m}$ , where  $d_0 = 430 \mu\text{m}$ .

antenna axis direction as the desired transmitter. The horizontal dashed line shows the not allowed positions for the interfering transmitter. For the case of  $h_{\text{slb}} = 4 \mu\text{m}$ , the distance between two transmitters must be greater than  $380 \mu\text{m}$  (the horizontal line length), while for the case with  $h_{\text{slb}} = 6 \mu\text{m}$  this distance increases to  $430 \mu\text{m}$ . It can be described by the fact that the multipath component decreases for smaller  $h$ , therefore the interference power decays more rapidly for the case with  $h_{\text{slb}} = 4 \mu\text{m}$ , as seen in Figure 4.

In Figure 10,  $G = 25$  dB,  $h_{\text{slb}} = 6$  and  $d_0 = 430 \mu\text{m}$  are considered. In such case, despite the high value of  $d_0$  compared to Figure 9,  $P_b \leq 10^{-8}$  can be satisfied with  $\Delta \geq 43 \mu\text{m}$  to positioning the adjacent transmitter for a parallel wireless link. It can be observed that, the distance between two horizontally aligned transmitters is increased to  $1.470$  mm. In fact, by increasing the antenna gain to  $25$  dB, the received

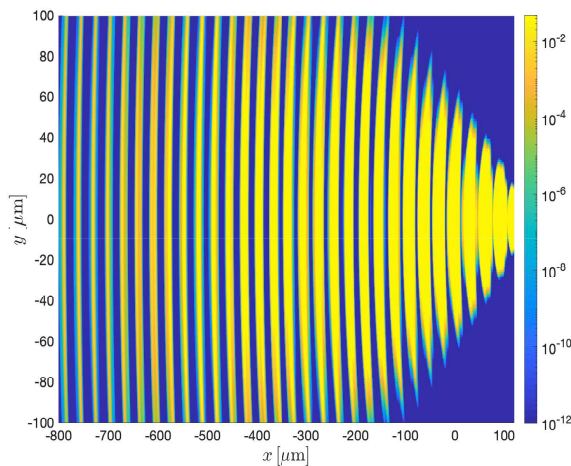


Figure 11. BEP vs position of TX<sub>1</sub> in the  $xy$  plane with  $G = 15$  dB,  $h_{\text{slb}} = 6$   $\mu\text{m}$ , where  $d_0 = 150$   $\mu\text{m}$ .

power by an interfering transmitter that is aligned horizontally to the desired transmitter decays significantly only at a large distance.

In Figure 11,  $G = 25$  dB and  $h_{\text{slb}} = 6$  with  $d_0 = 430$   $\mu\text{m}$  are considered. In such case, the optical system is subject to high fading, as shown in Figure 5 for the same  $G$  and  $h_{\text{slb}}$  without interference. Therefore, the results vs the positions of TX<sub>1</sub> show a marked non regularity for *not allowed* domain, as well as for *coverage* domain in Figure 5.

## VI. CONCLUSIONS

Optical wireless (OW) links as components of a network-on-chip (NoC) have been analyzed in the presence of multipath propagation, co-channel interference and noise. The wireless channel has been characterized by using a RT method applied to the on-chip scenario. The communication performance in terms of the BEP has been evaluated accounting for the statistics of random variables in the OW communication system. The effect of antenna directivity, geometrical parameters of the chip structure and wireless links, and the number of interfering links on the BEP have been investigated. Different link configurations have been examined, and the BEP has been plotted on grid maps with 1  $\mu\text{m}$  accuracy. The analysis helps determine supportable domains for the position of the link components, i.e., transmit and receive antennas, such that the required BEP is guaranteed. It has been shown that, for antennas with low directivity, the fading in OW channels can cause discontinuity in a supported domain. The fading is also subject to the thickness of the SiO<sub>2</sub> slab layer. Therefore, finding the optimal thickness for this layer can improve considerably the on-chip communication link performance.

## ACKNOWLEDGMENT

Research activity has been supported by PRIN 2015 Project “Wireless Networks through on-chip Optical Technology (WiNoT)”.

## REFERENCES

- [1] M. Nafari, L. Feng, and J. Jornet, “On-chip wireless optical channel modeling for massive multi-core computing architectures,” in *Proc. IEEE Wireless Commun. and Networking Conf.*, San Francisco, CA, USA, Mar. 2017, pp. 1–6.
- [2] G. Bellanca, G. Calo, A. E. Kaplan, P. Bassi, and V. Petruzzelli, “Integrated Vivaldi plasmonic antenna for wireless on-chip optical communications,” *Optics Express*, vol. 25, no. 14, pp. 16214–16227, Jun. 2017.
- [3] L. Benini and G. D. Micheli, “Networks on chips: a new SoC paradigm,” *IEEE Computer*, vol. 35, no. 1, pp. 70–78, Jan. 2002.
- [4] J. D. Owens et al., “Research challenges for on-chip interconnection networks,” *IEEE Micro*, vol. 27, no. 5, pp. 96–108, Nov. 2007.
- [5] J. Kim, K. Choi, and G. Loh, “Exploiting new interconnect technologies in on-chip communication,” *IEEE J. Emerg. Select. Top. Circuits Syst.*, vol. 2, no. 2, pp. 124–136, Jun. 2012.
- [6] A. Biberman and K. Bergman, “Optical interconnection networks for high-performance computing systems,” *Reports on Progress in Physics*, vol. 75, no. 4, pp. 046402–046416, Apr. 2012.
- [7] S. Werner, J. Navaridas, and M. Luján, “A survey on optical network-on-chip architectures,” *ACM Comput. Surv.*, vol. 50, no. 6, pp. 89:1–89:37, Dec. 2017.
- [8] M. A. I. Sikder, A. K. Kodi, M. Kennedy, S. Kaya, and A. Louri, “OWN: Optical and wireless network-on-chip for kilo-core architectures,” in *IEEE 23rd Annu. Symp. High-Perform. Interconnects*, Santa Clara, CA, USA, Aug. 2015, pp. 44–51.
- [9] D. DiTomaso et al., “A-WiNoC: Adaptive wireless network-on-chip architecture for chip multiprocessors,” *IEEE Trans. Parallel Distrib. Syst.*, vol. 26, no. 12, pp. 3289–3302, Dec. 2015.
- [10] M. O. Agyeman et al., “A resilient 2-D waveguide communication fabric for hybrid wired-wireless NoC design,” *IEEE Trans. Parallel Distrib. Syst.*, vol. 28, no. 2, pp. 359–373, Feb. 2017.
- [11] S. Abadal, A. Mestres, J. Torrellas, E. Alarcón, and A. Cabellos-Aparicio, “Medium access control in wireless network-on-chip: A context analysis,” *IEEE Commun. Mag.*, vol. 56, no. 6, pp. 172–178, Jun. 2018.
- [12] S. Abadal, A. Mestres, M. Nemirovsky, H. Lee, A. González, E. Alarcón, and A. Cabellos-Aparicio, “Scalability of broadcast performance in wireless network-on-chip,” *IEEE Trans. Parallel Distrib. Syst.*, vol. 27, no. 12, pp. 3631–3645, Dec. 2016.
- [13] J.-J. Lin, L. Gao, A. Sugavanam, X. Guo, R. Li, J. E. Brewer, and K. K. O, “Integrated antennas on silicon substrates for communication over free space,” *IEEE Electron Device Lett.*, vol. 25, no. 4, pp. 196–198, Apr. 2004.
- [14] H. K. Mondal, S. H. Gade, M. S. Shamim, S. Deb, and A. Ganguly, “Interference-aware wireless network-on-chip architecture using directional antennas,” *IEEE Trans. Multi-Scale Comput. Syst.*, vol. 3, no. 3, pp. 193–205, Jul. 2017.
- [15] F. Fuschini, M. Barbiroli, M. Zoli, G. Bellanca, G. Calò, P. Bassi, and V. Petruzzelli, “Ray tracing modeling of electromagnetic propagation for on-chip wireless optical communications,” *J. Low Power Electron. Appl.*, vol. 8, no. 4, pp. 39–54, Oct. 2018.
- [16] D. Matolak, S. K. A. Kodi, D. D. Tomaso, and W. R. S. Laha, “Wireless networks-on-chips: architecture, wireless channel, and devices,” *IEEE Wirel. Commun.*, vol. 19, no. 5, pp. 58–65, 2012.
- [17] D. Vantrease et al., “Corona: System implications of emerging nanophotonic technology,” in *Int. Symposium on Computer Architecture*, Beijing, China, Jun. 2008, pp. 153–164.
- [18] J. Shafiei Dehkordi and V. Tralli, “Interference analysis for optical wireless interconnections,” in *Proc. IEEE Int. Symp. on Personal, Indoor and Mobile Radio Commun.*, Bologna, Italy, Sep. 2018, pp. 1–7.
- [19] G. P. Agrawal, *Lightwave Technology: Telecommunication Systems*. Hoboken, NJ: Published by John Wiley & Sons, Inc., 2005.

# High Circular Dichroism through Planar Plasmonic Metasurfaces and Enhancement through Surface Plasmon Resonances

Badrul Alam, Vincenzo Petruzzelli

Department of Electrical and Information Engineering,  
Polytechnic University of Bari  
Bari, Italy  
Email: Badrul.Alam@poliba.it,  
Email: Vincenzo.Petruzzelli@poliba.it

Luca Maiolo

Institute for Microelectronics and Microsystems  
CNR-IMM  
Rome, Italy  
Email: luca.maiolo@cnr.it

Lorenzo Dominici, Francesco Todisco, Milena De Giorgi

Institute of Nanotechnology  
CNR NANOTEC,  
Lecce, Italy  
Email: lorenzo.dominici@gmail.com,  
Email: francesco-todisco@cnr.it,  
Email: milena.degiorgi@nanotec.cnr.it

Andrea Veroli, Alessio Benedetti

Department of Information Engineering, Electronics and  
Telecommunications,  
Sapienza, University of Rome  
Rome, Italy  
Email: Andrea.Veroli@uniroma1.it ,  
Email: Alessio.Benedetti@uniroma1.it

Giorgio Pettinari, Annamaria Gerardino

Institute for Photonics and Nanotechnologies  
IFN-CNR  
Rome, Italy  
Email: giorgio.pettinari@cnr.it  
Email: annamaria.gerardino@cnr.it

**Abstract**— Research on metasurfaces featuring high circular dichroism has been very active in the last decade, because of possible applications in various fields, such as spintronics, polarization optics and stereochemistry. Despite literature displaying various proposed geometries and methods, today it is hard to define an alternative choice combining high Circular Dichroism (CD), easy realization and robustness of performance. In this work, we show the design approach and first experimental demonstration of a planar plasmonic metamaterial based on a comma-shaped geometry, which can be used to obtain high CD. Our metasurface combines intrinsic chirality and enhancement effects due to high field localization. In particular, the relative correspondence between numerical analyses and experiments shows the possibility to tune the effects of Surface Plasmon Resonances to a certain extent. This is equivalent to the possibility of engineering stable peak values on specific wavelength ranges, even in the presence of geometrical non-idealities due to fabrication. Samples were built through standard top-down fabrication procedures, helped by the symmetry of the extrusion. The ease in implementation, combined with reliable performances, make our proposed metamaterial eligible for adoption for further research in high precision spectroscopy and optical manipulation at industrial scale.

**Keywords**—Circular Dichroism; Metamaterials; Plasmonics; Surface Plasmons; Microfabrication.

## I. INTRODUCTION

Chirality refers to the geometric property of a structure lacking mirror symmetry planes. It exists in many forms in nature, ranging from molecules to proteins and crystals. In contrast, a structure is achiral if it is indistinguishable or superimposable on its mirror image. Due to the interest in chiral molecules, optical dichroism properties of natural and artificial materials have become a hot research topic. CD of a specific material is of interest also for other applications, such as spintronics, polarization optics and negative refractive index. It consists in the difference in optical behavior, read as transmission or absorption, to circularly polarized optical waves. Various conventions can be used to quantify CD; between all those, we prefer the approach that values more the relative relations between the two polarizations, and we put in a second order of importance the amount of transmission (this increases the alternatives):

$$CD=(T_R-T_L)/(T_R+T_L); \quad (1)$$

where  $T_L$  and  $T_R$  are left and right polarization transmission spectra, respectively.

Literature on high CD metasurfaces is rich, and various alternatives have been developed and experimentally demonstrated [1]. Research can be categorized by the

working principles (extrinsic dichroism, intrinsic dichroism, or enhancements by field localization), but, over time, the main categorization discriminant has been the fabrication method [2], because of the need to single out the most reproducible and the best performing geometries. To the great variety of geometries that have been demonstrated corresponds a big variety of fabrication techniques and approaches, both top-down and bottom-up. In general, in quantitative terms of circular dichroism factor, the top-down approach is usually more successful. Notable three dimensional (3D) nanophotonic structures are the nanohelices [3] built with focused-ion-beam-induced-deposition technique or laser writing. Stacked planar (e.g., [2]) geometries are also present in literature, and such approach also allows to accomplish strong chiroptical responses; all of them can be built by combining lithography with alignment in a layer-by-layer manner. Other than 3D and stacked 2D structures, a few simple planar structures have been successful plasmonic gammadions, nanoslit pairs, split rings, and a few others [2] can be obtained with established and standardized fabrication techniques, although with a small CD factor due to the fact that thickness is significantly lower wavelength. An interesting approach is the structure obtained by a vertical extrusion of a 2D shape, which consists in the thick deposition of a 2D patterned geometry. With this concept, it has been possible to increase the intrinsic dichroism and obtain a “giant” CD in [4]. Unfortunately, the related bandwidth is very thin and it is possible to verify that such geometry has very feeble stability, as CD peaks may vary in amplitude and central wavelength. Overall, between all the options, it is hard to find one combining high CD, reliable performances, reproducibility and accessible fabrication. In [5], the authors present a structure featuring high CD values, obtained by combining a high intrinsic dichroism due to vertical extrusion with enhancements effects due to high field localization caused by Surface Plasmon Resonances (SPRs).

In this work, we extend the work in [5] and present the related design approach and the first experimental results. We have built “comma”-shaped geometries based on noble metals (Ag and Au), after an accurate design focused on the stability of performance. The fabrication was operated through a top-down approach by using a single lithographic step to imprint the geometric shapes; the thickness of the deposited material was significant (equivalent to 1-3 tenth of the wavelength). In line-transmission measurements helped to study the performances. We also show that, to a certain extent, it is possible to control the effects of SPRs, since there is a relative convergence between numerical results and experiments.

In Section II, the available experimental works and tools are presented. Those represent the framework of the design process, which is described in Section III. In Section IV, we show and compare the numerical and experimental results and provide related discussions. In the final section, the conclusions are drawn.

## II. EXPERIMENTAL METHODS AND TOOLS

Before dealing with the design, we first focus on the available experimental tools. Our goal was to define structures that can be built with standardized techniques and accessible tools. We thus decided to operate with a single step of 2D lithography (more specifically, we used Electron Beam Lithography) and lift-off process to pattern the evaporated metals. Depending on the available instruments, we decided the thicknesses of Ag and Au to be around 140 nm and 80 nm, respectively. As said previously, we fabricated two classes of metamaterials; the first was made of Ag, while the second class was made of Au, which was selected for its chemical stability and for its potential use as substrate for biological experiments.

Since the goal was to simplify the use of our metasurface, we decided to work with transmission

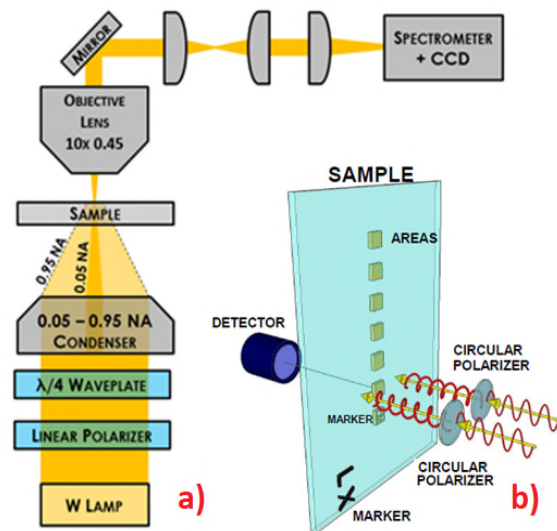


Figure 1. a) Shows the characterization setup used for the transmission analysis. The beam could reach areas down to 20  $\mu\text{m}^2$ . b) Layout of the samples, which contain various areas.

measurements, which allow to use setups that are easier to integrate. That said, we still wanted to show the performances of this structure with precision, so we used the setup used in Figure 1a-b. Figure 2 shows a Scanning

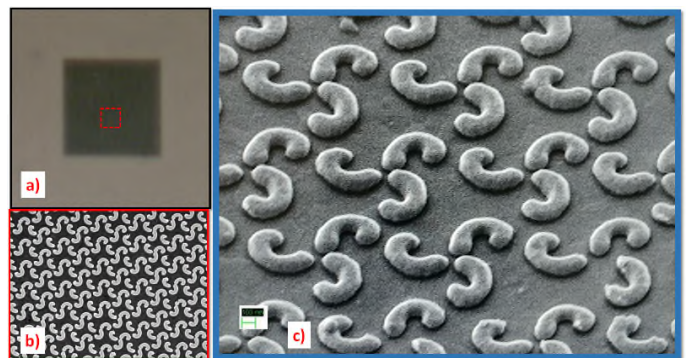


Figure 2. a) Image of an area, as seen under the microscope. b) SEM image representing the tip view. c) SEM image showing the oblique view of nano-commas; in particular, the curved lateral faces are visible.

Electron Microscopy (SEM) image of the Au sample whose experimental results are shown in this work.

### III. DESIGN APPROACH FOR NANOCOMMAS

Having defined the fabrication and characterization requirements and limits, we then proceeded to the design of the samples. We first searched for a shape lacking sharp edges and showing a degree of intrinsic CD; the avoidance of edges helps to reduce the variability of performances and eases the fabrication requirements. Between the plethora of possible geometries, we selected those which could be easily replicated with standard Electron Beam Lithography (EBL) processes, and could be distributed with high density on a surface. After some tests with the EBL, we heuristically chose a comma shaped geometry.

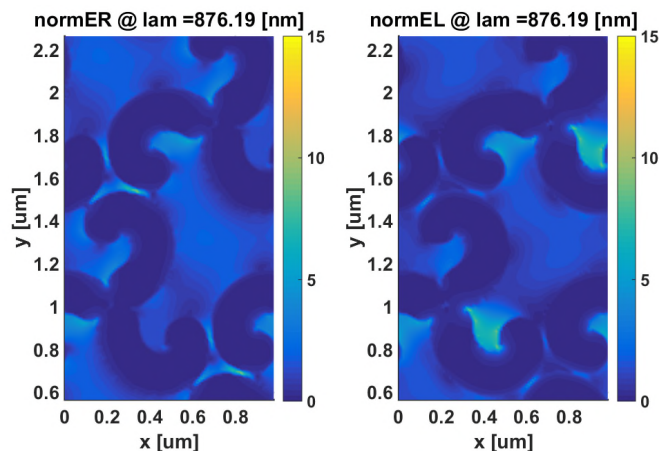


Figure 3. Example of field localization of the two types of polarization. Those concentrate on different sections of the nanocommas, depending on the circular polarization of the light (top is Right, bottom is Left).

The metamaterial in sample Ag was created after setting the “commas” in “triplets”, and those were then further inserted in triangular super-grids. The numerical methods and the specific operations used for the design are shown in [5], and the resulting grid cell is shown in Figure 3, along with an example of the field localization.

The Au sample was designed with a further evolution of the previous approach, as shown in [5]. This time, the “comma” shape was represented with the geometrical parameters of Archimedean spirals, and those parameters were weighted with their estimated variability after fabrication. Various numerical analyses were performed in order to find equilibrium situations where CD peaks were relatively constant.

### IV. RESULTS AND DISCUSSIONS

Some results from the Ag sample are shown in Figure 4. As can be seen, even though the resulting CD is relatively high, the amplitude varies significantly when different surfaces are tested (the regions shown in the image represent the tested positions). This means that there is a strong variability of the performance, even in the presence of small variations. Still, the central wavelength of the peaks is

conserved, and this satisfies one of the main objectives of the design.

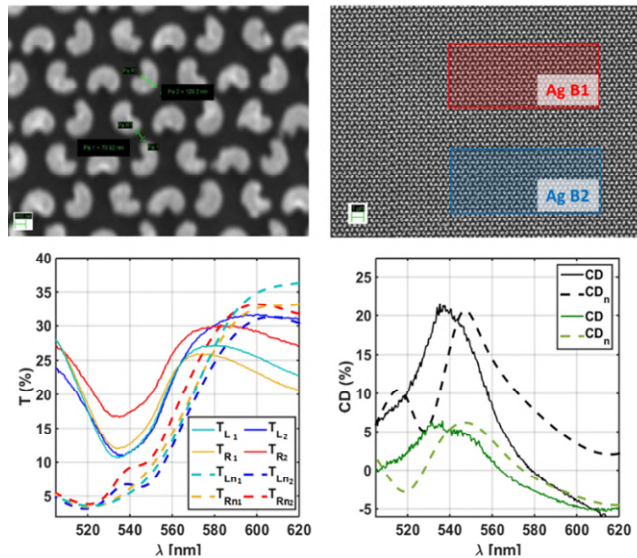


Figure 4. Top-Left: SEM image of the Ag sample’s layout Top-Right: A symbolic representation of the characterization on two different surfaces in the same metamaterial area (which should have the same geometry).

Bottom-Left: Transmission of the two polarizations according to numerical methods (dashed lines) and experiments (full lines); areas B1 and B2 are represented with indexes 1 and 2. Bottom-Right: Circular Dichroism calculated numerically (dashed lines) vs. experiments (full line); black lines correspond to area B1, while green lines correspond to area B2.

An extract from the first Au sample’s characterization is shown in Figure 5. As can be seen, the peaks are stable, since they are similar in amplitude and the peaks are around the same central wavelength. Unfortunately, the amplitudes of the CD peaks are lower than the expectations. This is probably due to the fact that this sample, as shown in Figure 1c, has round lateral profile due to a non-ideality in fabrication, while our design expected an extrusion of the same shape. Thus, the resonance at different heights is different, and this does not help to compose an overall strong CD.

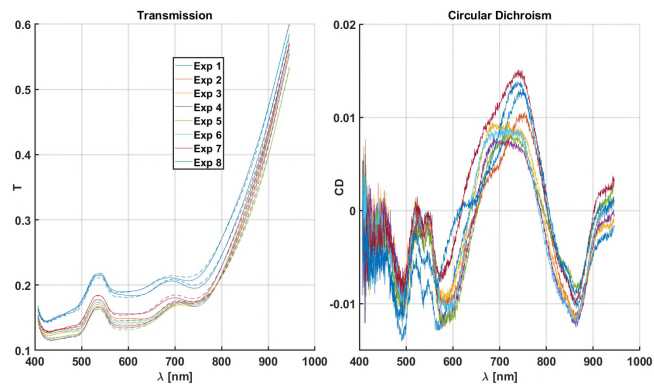


Figure 5. Left: Transmission of the two polarizations according to numerical methods and experiments. Right: Circular Dichroism calculated numerically vs. experiments

## V. CONCLUSIONS

In this work, we have shown that Surface Plasmon based metamaterials may reach high levels of linear CD, if we combine intrinsic chirality with enhancements due to Surface Plasmon Resonances. Our structure can be obtained with standard planar fabrication processes and involves the vertical extrusion of a planar shape, which has soft edges.

The design process succeeded in fixing the central wavelength, although the heuristic approach of the Ag sample revealed a variable amplitude depending on the lit area, while the Au sample revealed a more stable behavior, as per design. Thus, the parametrization of the geometry and the weighted sweep can be seen as viable strategy. Unfortunately, the Au sample presented here had a relatively small CD, due to a limited thickness and a curved lateral profile, as shown in oblique SEM images.

Overall, this class of metamaterials has shown potentialities and deserves more attention and research. In particular, Au samples with higher thickness values are now under investigation. The relative correspondence between numerical analyses and experiments shows the possibility to further develop this design method, which consists mainly

in finding stable peaks in Surface Plasmon Resonances. The reliability in results and the repeatability and scalability of this metasurface makes it interesting for its adoption for further research or industrial applications.

## REFERENCES

- [1] Z. Wang, F. Cheng, T. Winsor and Y. Liu, "Optical chiral metamaterials: a review of the fundamentals, fabrication methods and applications", *Nanotechnology*, vol. 27, pp. 412001-412021, 2016.
- [2] T. Tanaka and A. Ishikawa, "Towards three-dimensional optical metamaterials", *Nano Convergence*, vol. 4, is. 34, 2017.
- [3] A. Benedetti et al., "Precise detection of circular dichroism in a cluster of nano-helices by photoacoustic measurements", *Scientific reports*, vol. 7, pp. 5257, 2017.
- [4] A. Y. Zhu et al., "Giant intrinsic chiro-optical activity in planar dielectric nanostructures," *Light. Sci. & Appl.*, vol. 7, pp. 17158, 2018.
- [5] A. Veroli et al., "Planar chiral plasmonic 2d metamaterial: Design and fabrication", *AIP Conference Proceedings*, vol. 2145, pp. 020015, 2019.